

# Large cargo transport by nuclear pores: implications for the spatial organization of FG-nucleoporins

Li-Chun Tu<sup>1</sup>, Guo Fu<sup>1</sup>, Anton Zilman<sup>2</sup>  
and Siegfried M Musser<sup>1,\*</sup>

<sup>1</sup>Department of Molecular and Cellular Medicine, College of Medicine, The Texas A&M University, College Station, TX, USA and <sup>2</sup>Department of Physics, University of Toronto, Toronto, Ontario, Canada

Nuclear pore complexes (NPCs) mediate cargo traffic between the nucleus and the cytoplasm of eukaryotic cells. Nuclear transport receptors (NTRs) carry cargos through NPCs by transiently binding to phenylalanine-glycine (FG) repeats on intrinsically disordered polypeptides decorating the NPCs. Major impediments to understand the transport mechanism are the thousands of FG binding sites on each NPC, whose spatial distribution is unknown, and multiple binding sites per NTR, which leads to multivalent interactions. Using single molecule fluorescence microscopy, we show that multiple NTR molecules are required for efficient transport of a large cargo, while a single NTR promotes binding to the NPC but not transport. Particle trajectories and theoretical modeling reveal a crucial role for multivalent NTR interactions with the FG network and indicate a non-uniform FG repeat distribution. A quantitative model is developed wherein the cytoplasmic side of the pore is characterized by a low effective concentration of free FG repeats and a weak FG-NTR affinity, and the centrally located dense permeability barrier is overcome by multivalent interactions, which provide the affinity necessary to permeate the barrier.

*The EMBO Journal* (2013) 32, 3220–3230. doi:10.1038/emboj.2013.239; Published online 8 November 2013

**Subject Categories:** membranes & transport

**Keywords:** avidity; diffusion; FG nucleoporins; nuclear pore complex; single molecule fluorescence

## Introduction

Nuclear pore complexes (NPCs) facilitate bidirectional macromolecular traffic across the nuclear envelope (NE) (for reviews, see Stewart, 2007a; Wentz and Rout, 2010 and Jamali *et al*, 2011). Hundreds of proteins, RNA particles, and metabolites interact with and/or pass through each NPC every second (Hurt *et al*, 2000; Ribbeck and Görlich, 2001). The vertebrate NPC is ~120 nm in diameter and extends ~200 nm along the transport axis due to cytoplasmic filaments and a nuclear basket structure (Stoffler *et al*, 1999;

Fahrenkrog and Aebi, 2003). In humans, the hourglass-shaped central pore (or channel) has a minimum diameter of ~50 nm and a length of ~85 nm (Maimon *et al*, 2012). A network of ~250–300 intrinsically disordered polypeptide domains anchored to the NPC scaffold occupies the central channel and decorates the internal and external openings (Suntharalingam and Wentz, 2003; Lim *et al*, 2008b; Peleg and Lim, 2010). Together, these disordered nuclear pore proteins (nucleoporins or Nups) contain thousands of phenylalanine-glycine (FG) repeats to which soluble nuclear transport receptors (NTRs) transiently bind during transport. The FG network has an effective mesh size of ~4–5 nm, allowing small molecules (< ~30 kDa) to diffuse through in a signal-independent manner (Mohr *et al*, 2009). Larger cargos are carried through NPCs by NTRs, after recognition of a cargo's nuclear localization signal (NLS) or nuclear export signal (Chook and Süel, 2011; Güttler and Görlich, 2011). In the nucleus, RanGTP promotes disassembly of import complexes, freeing the cargo and allowing NTRs to diffuse back to the cytoplasm (Chook and Blobel, 2001). In the cytoplasm, export complexes are disassembled by RanGAP and Ran binding proteins (RanBPs) (Bischoff *et al*, 1994; Bischoff and Görlich, 1997; Kutay *et al*, 1997).

Numerous models describing the spatial distribution, conformations, and possible interactions of the FG polypeptides have been proposed to explain the NPC transport mechanism. There are several basic principles on which all these models agree, such as the facts that the intrinsically unfolded FG polypeptides provide the necessary binding sites for NTR-cargo complexes, and that these polymers are arranged on a scaffold of approximately cylindrical geometry. However, several points of contention remain. The polymer brush model postulates that the FG polypeptides are largely non-interacting, extended, and unentangled (Lim *et al*, 2006). In a contrasting model, the polymers are posited to exhibit a significant interstrand affinity, which results in a connected network resembling a hydrogel (Frey and Görlich, 2007). In addition, the arrangement of the FG polypeptides on the NPC scaffold and the distribution in space of their extended unfolded domains are still unclear, although it is clear that their density is quite high, at least in some regions. If all of the FG polypeptides were located within the central pore of the NPC, then they would occupy ~20% of the available space (hydration would increase the occupied volume significantly) (Peleg and Lim, 2010; Tu and Musser, 2010).

Proposed mechanisms of transport also make specific assumptions regarding the distribution of the FG polypeptides within the NPC. In the hydrogel model, the FG network is distributed throughout the whole cross-section of the central pore of the NPC, and small cargos diffuse through spaces within the flexible meshwork (Ribbeck and Görlich, 2001; Mohr *et al*, 2009). An alternative hypothesis is that small cargos diffuse through a relatively un-occluded region

\*Corresponding author. Department of Molecular and Cellular Medicine, Texas A&M University, TAMHSC College of Medicine, 1114 TAMU, College Station, TX 77843, USA. Tel.: +1 979 862 4128; Fax: +1 979 847 9481; E-mail: smusser@tamu.edu

Received: 23 May 2013; accepted: 1 October 2013; published online: 8 November 2013

of ~10 nm diameter in the middle of the central channel (Keminer and Peters, 1999; Yamada *et al*, 2010; Ma *et al*, 2012). It is also important to consider the nuclear and cytoplasmic edges of the NPC, where the conformation and arrangement of the FG polypeptides can differ significantly from those in the middle of the pore. These edge regions are important since transport complexes are assembled and disassembled during transport at both the nuclear and cytoplasmic openings (Stewart, 2007b; Sun *et al*, 2008, 2013; Jamali *et al*, 2011). For instance, integrating biophysical and bioinformatics data, the two-gate model (Patel *et al*, 2007) postulates brush-like structures on both cytoplasmic and nuclear sides of the NPC, suitable for binding and (dis)assembly reactions, and a central cohesive structure in the centre of the pore that provides the permeability barrier. Consistent with this picture, immunogold electron microscopy studies on the yeast NPC demonstrated that more than half of the FG-Nups are distributed on the two sides of the NPC at a distance of ~20–60 nm from the centre (Rout *et al*, 2000).

A major question is how NTR–cargo complexes (especially large ones), consisting of cargo and NTR molecule(s), are able to rapidly and locally displace the FG network allowing for fast translocation without collapsing the permeability barrier. For instance, the nuclear protein nucleoplasmin, which mediates nucleosome assembly, is a pentamer, and thus contains five NLSs, each of which can bind an NTR. Pentamers with a single NLS enter nuclei at about a 10-fold slower rate than those with five NLSs (Dingwall *et al*, 1982). The importance of multiple transport signals was also examined with a synthetic cargo containing two different NLSs that recognize different NTRs. In this case, both NTRs were required for rapid transport (Ribbeck and Görlich, 2002). For both of these studies, it is unclear whether slower nuclear uptake was a consequence of slower translocation through the pore (which could block or hinder the transport of other molecules) or whether cargos with only one NTR were largely rejected by the pore (aborted transport).

Single molecule studies are ideally suited to directly address this question. We demonstrate here using single particle tracking that large cargos with a single NTR readily bind to the cytoplasmic face of the NPC, but that efficient transport through the permeability barrier requires multiple NTRs. Surprisingly, however, a major increase in import efficiency is not accompanied by a substantial increase in residence time, indicating, as we show, that little time is spent transiting the permeability barrier region.

## Results

### The approach

We used narrow-field epifluorescence (Yang *et al*, 2004; Yang and Musser, 2006b) to directly monitor the nuclear import of a beta-galactosidase ( $\beta$ Gal) model cargo in permeabilized cells with a 500-Hz imaging rate and ~44 nm resolution (Supplementary Methods; Supplementary Figure S1). Fully labelled wild-type M9- $\beta$ Gal-16C cargo (Lyman *et al*, 2002) transported through NPCs in a signal-independent fashion (Supplementary Figure S2), and hence was unsuitable for our experiments. Therefore, a suitable signal-dependent model cargo was generated by four point mutations that reduced the

catalytic and binding activity towards disaccharides and lowered the number of cysteines available for fluorescent dye labelling (Materials and methods; Supplementary Figure S2). The resulting cargo, M9- $\beta$ Gal-8C, is an ~500 kDa tetramer (~18 × 15 × 9 nm) with four M9 NLSs that are recognized by the transportin (importin  $\beta$ 2) NTR. Gel filtration chromatography and single molecule photobleaching experiments indicate that up to four transportin molecules can simultaneously bind to M9- $\beta$ Gal-8C (Supplementary Figure S3). Nuclear import of M9- $\beta$ Gal-8C, labelled with eight Alexa647 dye molecules, requires transportin but not RanGTP (Figures 1A and B). NPCs were fluorescently tagged with GFP at the N-terminus of the pore membrane protein, Pom121, a centrally located Nup (Brohawn *et al*, 2009). The N-terminus of Pom121 is not accessible to antibodies in permeabilized cells, suggesting that this portion of the protein is located in the ER lumen, and hence, not within the FG network (Söderqvist and Hallberg, 1994), and therefore, that GFP tags on this part of Pom121 are unable to interfere with the binding of NTR–cargo complexes within the FG network. Cargo transport trajectories were determined relative to the NE using the GFP fluorescence of labelled Pom121 (Figure 1C, Supplementary videos 1 and 2).

Single-molecule nuclear import experiments were performed largely as described earlier (Yang *et al*, 2004; Yang and Musser, 2006a, b), with minor modifications as described in detail in Materials and methods and Supplementary data. Three major experimental parameters were measured: (1) *interaction time* was obtained by fitting a histogram of NPC residence times to a first-order exponential equation; (2) *import efficiency* (defined as the (number of entry events)/(number of abortive and entry events)) is the percentage of NPC binding events for which a cargo enters the nucleus; and (3) *interaction frequency* is the number of NPC interaction events per  $\mu$ m of NE per second.

### The import efficiency of M9- $\beta$ Gal-8C is lower than that of M9-2xGFP

The interaction time of M9- $\beta$ Gal-8C with the NPC in the presence of exogenous RanGTP and 1  $\mu$ M transportin was  $8.7 \pm 0.8$  ms, which is similar to that observed for a significantly smaller cargo (2xGFP, ~60 kDa,  $6.8 \pm 0.9$  ms) with the same M9 NLS (Figure 2A). However, the import efficiency of M9- $\beta$ Gal-8C is ~50% lower (Figure 2B), consistent with the hypothesis that a larger cargo has more difficulty crossing the permeability barrier.

### A single transportin receptor promotes binding but is insufficient for efficient nuclear transport

We next investigated the import of M9- $\beta$ Gal-8C as a function of the transportin: cargo ratio. In these experiments, the cargo concentration was fixed at ~0.1 nM. To preassemble transportin: cargo complexes, transportin and M9- $\beta$ Gal-8C were incubated together on ice for at least 20 min before addition to permeabilized cells (see Supplementary Table S1 for additional details). As the transportin: cargo (mol: mol) ratio was increased from 1:4 to 10 000:1, the import efficiency increased ~8-fold, from  $3 \pm 2$  to  $24 \pm 4\%$  (Figure 2C; Supplementary Table S1). In contrast, the interaction time increased only ~2-fold, from  $4.8 \pm 0.4$  to  $8.7 \pm 0.8$  ms (Figure 2D; Supplementary Table S1). Note that there was little difference in import efficiency and interaction time for a

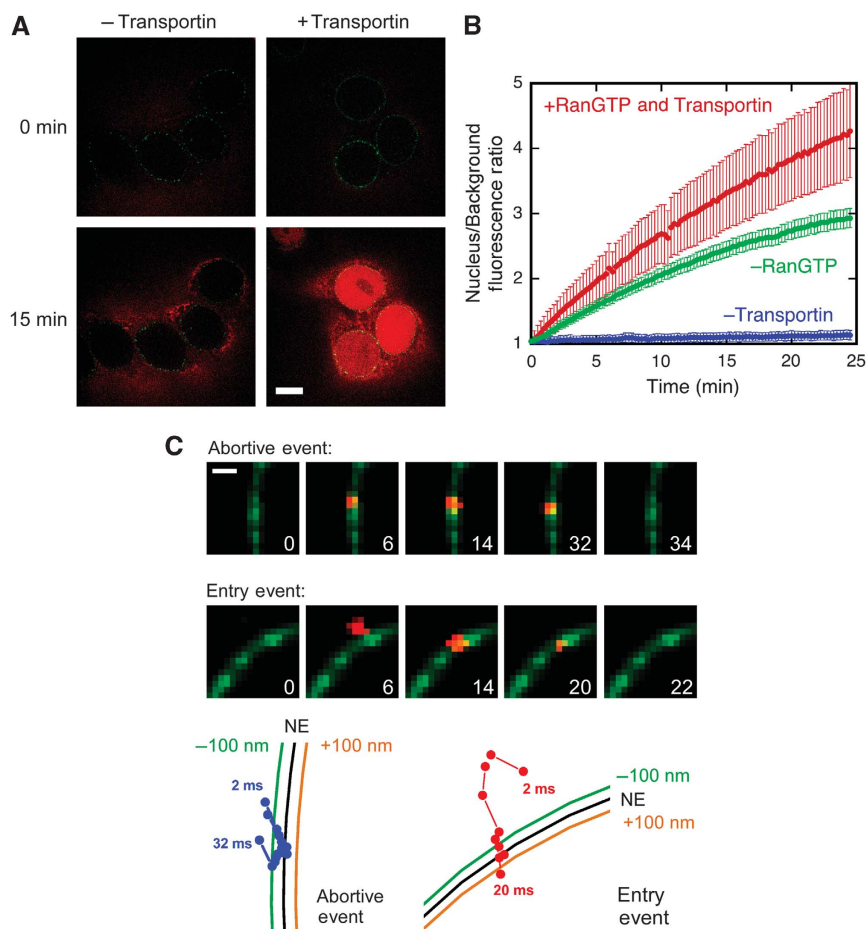


**Figure 1** Nuclear import of M9- $\beta$ Gal-8C. **(A)** Transportin-dependent nuclear import of M9- $\beta$ Gal-8C. Bar, 10  $\mu$ m. **(B)** Kinetics of nuclear import of M9- $\beta$ Gal-8C in the presence and absence of transportin and RanGTP, as indicated. For **(A, B)**, images were obtained by confocal microscopy. [transportin] = 1.0  $\mu$ M, [RanGDP] = 0.5  $\mu$ M, [GTP] = 1 mM, [NTF2] = 1  $\mu$ M, and [M9- $\beta$ Gal-8C] = 0.25  $\mu$ M. **(C)** Images (2 ms integration time) from abortive and entry events obtained via narrow-field epifluorescence microscopy. The green colour reveals the positions of NPCs in the NE of a permeabilized HeLa cell from the fluorescence of EGFP-rPom121, and the red colour arises from the M9- $\beta$ Gal-8C cargo. Numbers are time in milliseconds. Particle trajectories for the abortive and entry interactions are shown aligned to the NE position. Protein concentrations are the same as in the bulk experiments, except that [M9- $\beta$ Gal-8C]  $\approx$  0.1 nM. Bar, 1  $\mu$ m.

transportin: cargo ratio of 4:1 and higher, suggesting that any potential accumulation of transportin in the NPC that might have occurred at high transportin concentrations did not affect these parameters. These findings have important implications regarding the spatial conformations and distribution of the FG-Nups in the NPC (described later).

In the absence of exogenous transportin, the NPC interaction frequency decreased by  $\geq 10$ -fold, and therefore was essentially non-existent (Figure 2E; Supplementary Table S1). Thus, transportin is required for the cargo to bind to the NPC. Pre-treatment with RanGTP did not significantly reduce the NPC interaction frequency, confirming that binding resulted from the exogenous transportin rather than residual NTRs within the permeabilized cells (Supplementary Table S1). At a transportin: cargo ratio of 1:4, at most  $\sim 20\%$  of the cargo molecules had a single transportin molecule bound (calculated using the binding affinity of the cargo for the NTR), and no more than  $\sim 2\%$  of cargo molecules had two transportin molecules bound (Figure 2F; Supplementary Table S1). These data support a picture in which a single transportin molecule is sufficient for binding, but not for transport.

Surprisingly, NPC binding at the 1:4 transportin: cargo ratio was very low in the absence of RanGTP, precluding determi-

nation of an interaction time and import efficiency under these conditions. For an unknown reason, substantially fewer cargos reached the cytoplasmic space near the NE under these conditions, possibly due to unknown binding interactions within the cytoplasmic compartment. Pre-treatment of permeabilized cells with RanGTP to wash away any NTRs bound at cytoplasmic locations far away from the NE did not increase the NPC interaction frequency (Supplementary Table S1).

### Location of the permeability barrier

By analysing many transport trajectories, the locations within the NPC that are accessible to NTR-cargo complexes can be determined. Two-dimensional histograms were generated by calculating the frequency with which single molecule positions were observed at locations in and around an NPC. The peaks in these histograms indicate regions where the interacting particles spend most of the time. Specifically, we analysed the abortive trajectories at both high and low transportin: cargo ratios in order to determine the approximate location of the permeability barrier (Figure 3). It was not practical to obtain frequency maps for the nuclear entry events due to the infrequency of such events, especially at

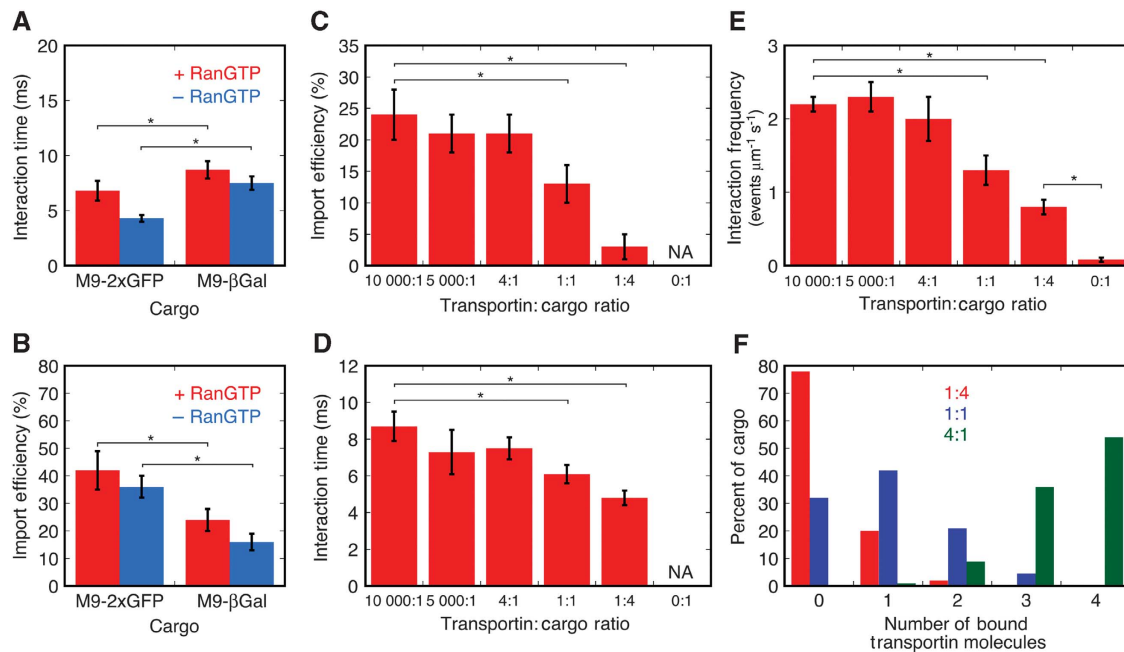


**Figure 2** Import efficiency and interaction time of M9-βGal-8C and 2xGFP cargos. (A, B) Comparison of interaction times and import efficiencies for M9-2xGFP and M9-βGal-8C in the presence and absence of RanGTP. (C, D) Dependence of interaction time and import efficiency for M9-βGal-8C on the transportin concentration. (E) Interaction frequencies. These data indicate that M9-βGal-8C cannot bind to NPCs in the absence of transportin. (F) Distribution of the number of bound transportin molecules in NTR-cargo complexes based on the binomial distribution. Important statistically different values at the 95% level (two-tailed Welch's *t* test—see Materials and methods) are identified by the stars (\*) and brackets. See Supplementary Table S1 for details. Conditions of Figure 1C for all panels, unless otherwise indicated.

low transportin concentrations. Construction of true density/concentration profiles requires knowing the accessible volume within the various regions, which likely varies based on the location along the transport axis due to structural constraints, and is unknown and difficult to obtain. Nonetheless, these data suggest that the permeability barrier is centrally located, estimated to be  $\sim 0 \pm 20$  nm from the reference plane determined by the location of Pom121. This is consistent with the recent finding that the permeability barrier involves Nup98, a centrally located cohesive Nup (Hülsmann *et al*, 2012).

#### Analysis of the effect of multivalency on import efficiency and transport time

Figure 2 indicates that M9-βGal-8C bound to multiple transportin receptors has a clear advantage in import efficiency. What is the source of this advantage? An obvious answer is that the cargo's overall affinity for the pore is higher due to multivalent interactions, that is, several transport receptors on the NTR-cargo complex can bind simultaneously to the FG network, and that this allows for easier penetration of the permeability barrier. The affinity due to multivalent interactions is known as 'avidity' (Kindt *et al*, 2007).

The expectation for an NTR-cargo complex with multiple simultaneous binding interactions with the FG polypeptides is that its rate of release from the FG network, and thus from the NPC, should be slower than that of a molecule with a single binding interaction (see Supplementary data). Surprisingly, however, similar NPC interaction times were observed for M9-βGal-8C cargo complexes with either one or multiple bound transportin molecules (Figure 2D). One interpretation of this finding is that RanGTP is sufficiently available on the cytoplasmic face of the NPC and effectively

controls the rate of cargo release from the NPC. While RanGTP could leak through the NPC, this interpretation appears to be invalid since the M9-βGal-8C interaction time is statistically identical in the presence and absence of RanGTP (Figure 2A; Supplementary Table S1). An alternative explanation is therefore necessary to explain the similar interaction times at different transport concentrations.

#### Mathematical description of multivalent affinity (avidity) and implications

The paradoxical behaviour of multivalent NTR-cargo complexes in our experiments indicates several important properties of the nuclear transport process. To understand these, a mathematical description of the binding affinity of multivalent cargos is needed. To simplify the discussion, we assume that each transportin molecule on an M9-βGal-8C cargo complex can bind a single FG repeat. As described in Supplementary data, the results are readily extended and do not change substantially with multiple binding sites per NTR (Supplementary Figure S4). At any moment, a cargo with four bound transportin molecules can bind to one, two, three, or four FG repeats with each individual binding event characterized by the binding affinities (equilibrium dissociation constants)  $K_{D1}$ ,  $K_{D2}$ ,  $K_{D3}$ , and  $K_{D4}$ , respectively. In this situation, the apparent affinity (also known as avidity) of the complex for the FG network depends on the local availability, and thus the concentration,  $[F]$ , of the FG repeats. This apparent affinity is characterized by the apparent dissociation constant,  $K_{app}$  (see the derivation of Eq. S13 in Supplementary data for details):

$$K_{app} = \frac{K_{D1}}{1 + \frac{[F]}{K_{D2}} + \frac{[F]^2}{K_{D2}K_{D3}} + \frac{[F]^3}{K_{D2}K_{D3}K_{D4}}} \quad (1)$$



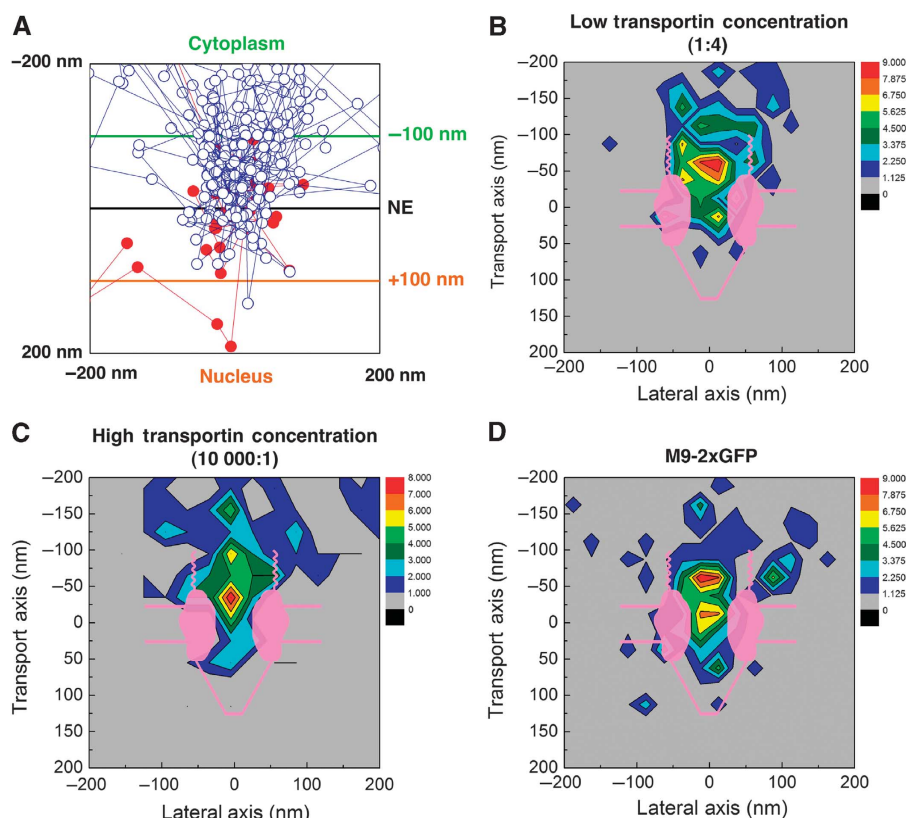


**Figure 3** Location of the permeability barrier. (A) Overlay of entry (red) and abortive (blue) trajectories obtained at a low transportin: cargo ratio (1:4) ( $N=37$ ). Under these conditions, most of the M9- $\beta$ Gal-8C molecules are bound to a single transportin molecule (Figure 2F). Trajectories were aligned as described in Supplementary data. (B, C) Density maps of M9- $\beta$ Gal-8C positions for abortive events at low (1:4) (B) and high (10 000:1) (C) transportin: cargo ratios ( $N=34$  and  $41$ , respectively). The map in (B) is from the data in (A). Abortive cargos spend very little time within the nuclear basket region, but a significant time within the cytoplasmic filament region. (D) Density map of M9-2xGFP positions for abortive events at a high (10 000:1) transportin: cargo ratio ( $N=54$ ). For (B–D), an NPC schematic is shown approximately to scale.

where  $K_{D1}$  is the binding affinity for the first FG repeat when there are four transportin molecules in the NTR–cargo complex. As discussed in Supplementary data, the values of the  $K_D$ 's depend on the number of NTRs in the NTR–cargo complex.

The local dissociation time is also affected by multivalent binding. The average time required for the NTR–cargo complex with four transportin molecules to dissociate from all bound FG repeats,  $\tau_{app}$ , relates to the average time for an NTR–cargo complex with only one transportin molecule to dissociate from a bound FG repeat,  $\tau_{off}$ , as follows (see the derivation of Equations 21 and 22 in Supplementary data for details):

$$\frac{\tau_{app}}{\tau_{off}} = \frac{K_{D1}}{K_{app}} = 1 + \left(\frac{[F]}{K_{D2}}\right) + \frac{4}{9} \left(\frac{[F]}{K_{D2}}\right)^2 + \frac{2}{27} \left(\frac{[F]}{K_{D2}}\right)^3 \quad (2)$$

Thus, both the apparent affinity and the local off-time depend on the concentration of the FG repeats and the FG–NTR interaction strength. The physics behind this dependence can be understood by examining two limits. If  $[F]/K_{D2} \ll 1$  (i.e.,  $\tau_{app}/\tau_{off} \approx 1$  and  $K_{app}/K_{D1} \approx 1$ ) (colloquially denoted as the ‘low avidity’ regime), then multivalency does not have significant effects on the binding affinity, because, on average and at any given time, only one of the NTRs in the complex is bound to an FG repeat. In the other limit,  $[F]/K_{D2} > 1$

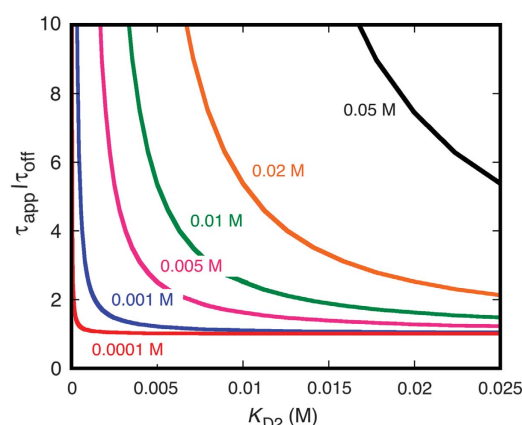


**Figure 4** Effect of FG concentration and NTR–FG affinity on the multivalent affinity of NTR–cargo complexes. The relationship between  $K_{D2}$  and  $\tau_{off}/\tau_{app}$ , according to Equation (2). The different FG concentrations,  $[F]$ , for the various curves are identified in colour.

(i.e.,  $\tau_{app}/\tau_{off} \gg 1$  and  $K_{app}/K_{D1} \ll 1$ ), all four NTRs are bound simultaneously to the FG repeats resulting in a higher apparent affinity (‘high avidity’ regime). The value of  $\tau_{app}/\tau_{off}$  is illustrated in Figure 4 as a function of  $K_{D2}$  and  $[F]$ .

While the lifetimes in Equation (2) describe the average time to release from the last FG repeat, they differ from the overall NPC interaction times since the latter include the time to diffuse out of and away from the FG network, which could be significant. Nonetheless, Equation (2) indicates conditions under which multivalency is expected to be significant. For example, when  $[F] \approx K_{D2}$ ,  $\tau_{app}/\tau_{off} \approx 2.5$ . Thus, the data in Figure 2D suggest that  $[F] < K_{D2}$  for NTR–cargo complexes with 1–4 bound transportin molecules, indicating similar off times and thus weak multivalency effects for the M9- $\beta$ Gal-8C cargo with four transportin molecules. This presents a serious conundrum since the total average FG concentration in the central pore is expected to be in the order of  $\sim 30$  mM (Stewart, 2007a; Peleg and Lim, 2010) and NTR affinities for an FG repeat are typically estimated to be in the micromolar range or less (Bayliss *et al*, 1999, 2002; Ben-Efraim and Gerace, 2001; Ribbeck and Görlich, 2001; Pyhtila and Rexach, 2003; Tetenbaum-Novatt *et al*, 2012). A solution to this issue is described below.

#### NTR-FG affinities and the distribution of FG repeats

Multiple transportin molecules are necessary for the M9- $\beta$ Gal-8C cargo complexes to efficiently cross the permeability barrier. A reasonable interpretation is that in order to efficiently penetrate the FG network, the enthalpic cost of disrupting any intra- or inter-polypeptide interactions and the entropic cost of disturbing the network must be compensated for by interactions of the NTR–cargo complex with the FG polypeptides. According to this picture, an NTR–cargo complex with multiple NTRs forms more compensating interactions, thus allowing it to more easily penetrate the barrier. More precisely, the total free energy of an NTR–cargo complex within the FG network is lower if the complex has a higher affinity for it. This concept is closely related to solubility, as pointed out earlier (Ribbeck and Görlich, 2001), regardless of the molecular description and the specific properties of the permeability barrier. To say that a molecule is soluble in a solvent or a heterogeneous material implies that the free energy of its interaction with it is negative (favourable). A major prediction of this model, however, is that an increased number of favourable interactions is expected to decrease the probability of

release, and thus increase the residence time of the interaction. That is, multivalent interactions are expected to result in a substantially higher overall affinity for the NPC, which should result in substantially longer interaction times. This was not observed, as pointed out earlier, as interaction times varied by only  $\sim 2$ -fold (Figure 2D) between low and high NTR: cargo conditions.

This discrepancy can be resolved if there is a spatially inhomogeneous distribution of the FG-Nups in the NPC. The trajectory data reveal that the overall interaction region of M9- $\beta$ Gal-8C with the NPC is significantly wider than the static spatial error ( $< 20$  nm) of our measurements, even for molecules that cannot penetrate the permeability barrier (Figure 3), indicating that aborted transport does not result simply from binding to and release from the surface of the permeability barrier. This indicates that the NTR–cargo complex can interact with FG polypeptides over an extended region of space at the cytoplasmic periphery of the pore (the cytoplasmic ‘vestibule’) before encountering the permeability barrier. In this picture, this ‘vestibule’ is characterized by a relatively sparse, low-density distribution of FG polypeptides (potentially with few inter-polypeptide interactions). In contrast, the central region is densely packed with FG polypeptides, thus establishing the permeability barrier. The free energy cost of penetrating this barrier can arise both from the entropic cost of displacing the dense FG-Nups and from the enthalpic cost of breaking a high number of cohesive interactions involving GLFG repeats (Patel *et al*, 2007) (Figure 5). As a consequence of these regions of different FG densities, multivalent interactions of the NTR–cargo complex with the FG network are expected when it is within the permeability barrier, while most of the transport time is spent in the low density cytoplasmic vestibule, where monovalent interactions dominate. Thus, although the multivalent interactions decrease the permeability barrier and significantly enhance the import efficiency, their effect on transport times is low. A quantitative description of this model is given in the next section.

Considering the bidirectional traffic through the NPC and the similar functions of the cytoplasmic filaments and the nuclear basket, it is likely that a nucleoplasmic vestibule exists, which, like the cytoplasmic vestibule, is characterized

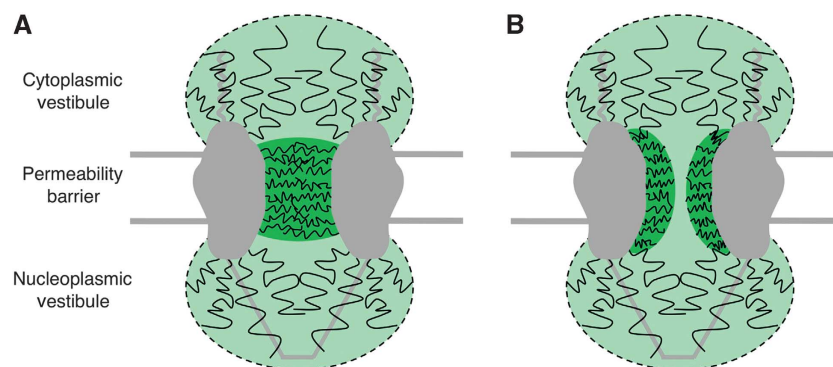


**Figure 5** Models of the distribution and density of FG polypeptides. Efficient binding but low import efficiency of the M9- $\beta$ Gal-8C cargo at a low transportin concentration indicates that the initial binding region and the permeability barrier are distinct entities with different properties. In these models, the permeability barrier comprises a relatively dense network of FG polypeptides in the central pore, whereas the cytoplasmic and nucleoplasmic vestibules contain sparser distributions of FG polypeptides. One possibility is a network that completely occludes the pore (A). Since the M9- $\beta$ Gal-8C cargo ( $18 \times 14 \times 9$  nm) (Jacobson *et al*, 1994) is too large to penetrate unassisted, a relatively unoccluded region in the middle ( $\sim 10$  nm diameter) is consistent with our data (B). See text for details.

by a low density distribution of FG polypeptides. This picture is consistent with numerous established results, including: (1) the accumulation of transport cargos at both the cytoplasmic and nucleoplasmic exits of the NPC (Feldherr *et al*, 1984; Richardson *et al*, 1988); (2) the regions of transport complex assembly and disassembly identified in single molecule fluorescence resonance energy transfer experiments (Sun *et al*, 2008, 2013); and (3) the density distribution map for mRNA molecules undergoing export (Siebrasse *et al*, 2012), which looks similar, except in reverse, to the maps in Figure 3. Note that this model predicts that transport complexes have easy access to soluble factors in the nucleoplasmic and cytoplasmic vestibules, which have been shown to be important for complex assembly and disassembly during transport (Sun *et al*, 2008, 2013).

From a structural standpoint, the FG domains as intrinsically unfolded chains are likely to adopt relatively diffuse, low density conformations at the pore peripheries, free from the confining effect of the structural scaffold (de Gennes, 1979). The specific molecular underpinning of the permeability barrier—whether a brush or gel or something else (Lim *et al*, 2008a), or whether the network is continuous across the pore or there is a relatively open hole (e.g., Figure 5)—is not critical to the model described herein.

#### Quantitative formulation of the model as diffusion in a double-well potential

In order to put the structural model outlined above onto a quantitative footing, we modelled cargo transport as diffusion in an effective free energy potential. The local values of the effective potential depend on the physical properties of the NTR-cargo complex and its interaction with the FG-Nups, and they are determined by the interaction strength of the NTR-cargo complex for the local FG network, and any enthalpic or entropic cost(s) of disrupting the network (Zilman *et al*, 2007). We assumed the effective potential shown in Figure 6, which has the following characteristics. In the absence of binding, the centrally located dense distribution of FG-Nups mounts an effective potential barrier of height  $E_b^\circ$  due to the entropic cost of displacing the FG polypeptides, and possibly, the enthalpic cost of breaking FG-FG interactions. A lower barrier,  $E_v^\circ$ , is present within the cytoplasmic and nucleoplasmic vestibules due to the sparser distribution of FG polypeptides. For simplicity, we assume that the cytoplasmic and nucleoplasmic vestibules are symmetrical. However, this is not essential for our conclusions, and the model can be readily modified. Binding interactions of NTRs with the FG repeats (largely enthalpic) lower the energy barrier felt by the NTR-cargo complex by an amount that depends on the number of bound NTRs, the affinity of the interaction(s), and the density of the FG repeats. Roughly speaking, the magnitude of the barrier reduction due to the binding interactions is proportional to  $-k_B T \ln(K_{app})$ , where  $K_{app}$  is the local apparent affinity within the barrier region, as described by Equation (1). An important feature of the model is that because the density of the FG-Nups is low in the vestibule region, the reduction in the barrier in this region is similar for the cargos with one or more NTRs ( $K_{app}/K_{D1} \approx 1$ ). However, in the permeability barrier region, the barrier reduction is more significant for the cargos with four bound NTRs due to multivalent binding, as follows from

Equation (1). This leads to the significant enhancement of import efficiency for cargos with multiple NTRs.

As the exact values of the NTR-FG interaction free energies and the valencies of the interactions in the various regions are not fully known, we investigated the predicted transport probabilities (efficiencies) and times as a function of  $E_v$ ,  $E_b$  and the widths of the different regions (see Supplementary data for details). The results are graphically summarized in Figure 6 and Supplementary Figures S5 and S6. Comparison of the experimental data with the theoretical calculations suggests that the height of the central permeability barrier,  $E_b$ , is of the order of 1–2  $k_B T$  for the cargos with one NTR and is reduced by about 3  $k_B T$  to about  $-1 k_B T$  for the cargos with many NTRs. The well depth of the vestibules,  $E_v$ , is affected less and decreases from about  $-2.5$  to  $-4 k_B T$  at low transportin concentration to about  $-3$  to  $-4.5 k_B T$  at high transportin concentration. This is the expected mathematical consequence of a similar average number of NTR-FG interactions in the vestibule regions for cargos with one or more NTRs. Similar values were obtained in the presence and absence of RanGTP. Thus, RanGTP does not substantially affect the binding interactions in the cytoplasmic vestibule or the central permeability barrier, as expected, but it can promote transport by catalysing complex disassembly within the nucleoplasmic vestibule, releasing the free cargo, which is unable to transit back to the cytoplasm. All of these values are consistent with the general picture outlined in the last paragraph and shown schematically in Figure 6. Note that this double-well potential model is a refinement of previous single-well potential models (Frey and Görlich, 2007; Zilman *et al*, 2007; Tu and Musser, 2010).

## Discussion

The results reported here, combined with the theoretical analyses, quantitatively elucidate the energetics of transport through the NPC. In addition, they provide important insights regarding the strength of FG-NTR interactions and the spatial distribution of the FG-Nup density within the NPC. Though central to fully understanding the energetics of transport, it is difficult to estimate the true transportin-FG interaction strength from the values discussed above since it is masked by other components of the free energy, that is, the cost associated with the displacement of the FG-Nups or other conformational changes and the potential costs of breaking any FG-FG interactions. In principle, the change in barrier height with the transportin concentration provides a measure of the binding energy of the additional NTR(s). However, it is unclear whether the change in barrier height from low to high transportin concentration is due to the binding of an additional 1, 2, or 3 transportin molecules. While four transportin molecules can feasibly be attached to the M9- $\beta$ Gal-8C cargo (Supplementary Figure S3), a relatively open region unoccluded by FG repeats (Figure 5B) (Keminer and Peters, 1999; Yamada *et al*, 2010; Ma *et al*, 2012) may make it difficult for all four NTRs to simultaneously bind to FG repeats. The cytoplasmic vestibule depth at a low transportin: cargo ratio provides a more direct measure of the enthalpy of an individual transportin-FG-Nup interaction, as there is likely a minimal displacement cost associated with binding in this region. Our free energy potential model predicts the strength of an individual transportin-FG interaction to be  $< 10 k_B T$ ,

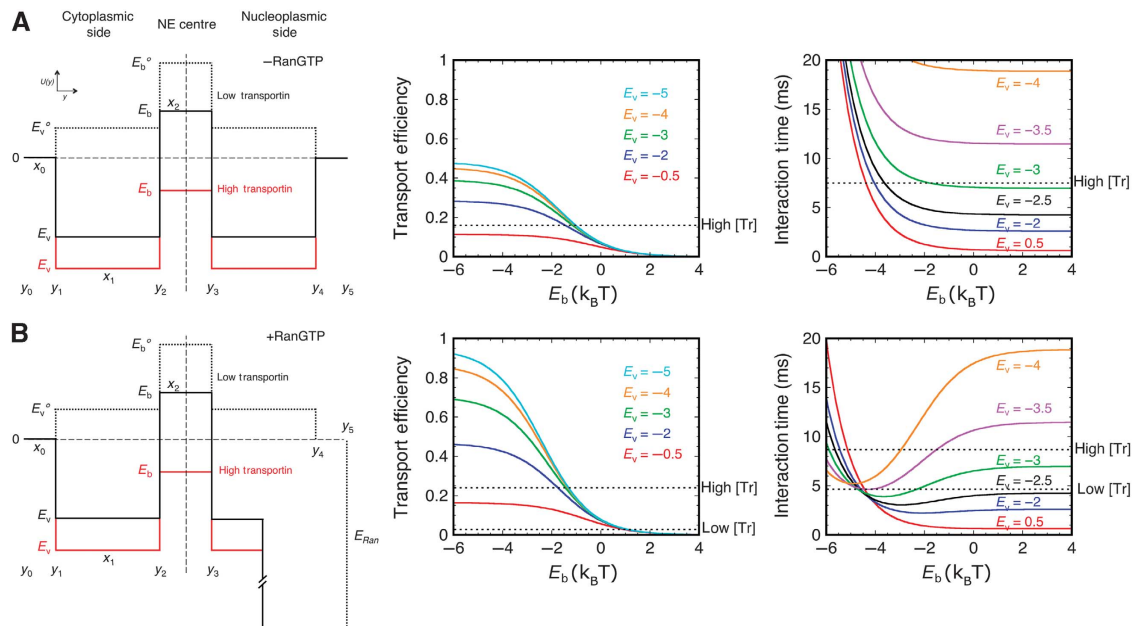


**Figure 6** Double-well diffusion model. The models in Figure 5 describe a significant free energy barrier for entry into the central region of the pore, and a relatively low barrier for entering the cytoplasmic and nucleoplasmic vestibules (*dashed black*). The cytoplasmic and nucleoplasmic vestibules are assumed to impart similar thermodynamic barriers, resulting in a symmetric potential in the absence of RanGTP (**A**). M9- $\beta$ Gal-8C requires multiple transportin molecules to efficiently lower and cross the central barrier (*red*), though binding and entry to the cytoplasmic vestibule is easily accomplished with a single transportin molecule (*solid black*). RanGTP promotes dissociation of import complexes, by strongly binding to the NTRs. This is modelled as a free energy sink in the nuclear basket region (**B**). The various  $y_i$  values indicate the boundaries of the regions with different properties along the transport axis and the  $x_i$  values indicate their widths. The barrier region width ( $2x_2$ ), vestibule width ( $x_1$ ), and escape distance ( $x_0$ ) are assumed to be 40, 80, and 25 nm, respectively (see Supplementary Figures S5 and S6 for other values). The RanGTP binding energy was assumed to be  $\sim 12$  k<sub>B</sub>T ( $\sim 7$  kcal/mol). Since GTP hydrolysis does not occur until recycling of the NTR back to the cytoplasm, this only approximates the binding energy. The results are relatively insensitive to the magnitude of this value, as long as it is large ( $\geq \sim 6$  k<sub>B</sub>T). The graphs show the import efficiency ( $P_{tr}$ ) and mean interaction times ( $\tau$ ) as a function of the barrier height ( $E_b$ ) for various well depths ( $E_v$ ) for a particle initially at  $y_1$ , as calculated in Supplementary data. Predicted values for  $E_b$  and  $E_v$  according to the experimental data vary by  $\sim 0.5$ – $1$  k<sub>B</sub>T if the barrier width is 20 nm (Supplementary Figures S5 and S6), as might be expected for the model in Figure 5B. Experimentally determined values (Supplementary Table S1) are indicated for low and high transportin (Tr) concentrations in the presence and absence of RanGTP by the horizontal dashed lines, as indicated. See text for details.

corresponding to a tens of micromolar to millimolar dissociation constant. This range of interaction strengths is consistent with the results of recent computational studies of the energetics of the transport through the NPC (Tagliazucchi *et al*, 2013) and the 25- $\mu$ M affinity for a single FG repeat estimated for NTF2 (Chaillan-Huntington *et al*, 2000). A weak transportin-FG interaction strength is required in our model to obtain millisecond transport times consistent with the data.

Numerous literature values for the affinities of NTRs for FG-Nups are substantially stronger (by an order of magnitude or more) than those derived from the quantitative analysis of the data by our model. Although varying considerably between different measurement methods, the dissociation constants typically lie in the micromolar to nanomolar range (Bayliss *et al*, 1999, 2002; Ben-Efraim and Gerace, 2001; Pyhtila and Rexach, 2003; Tetenbaum-Novatt *et al*, 2012), in particular,  $\sim 4$   $\mu$ M for transportin (Ribbeck and Görlich, 2001). The discrepancy between rapid translocation times and equilibrium affinities has been noted previously (Tetenbaum-Novatt *et al*, 2012). Several explanations for these discrepancies are possible. First, as discussed earlier, the apparent affinity of FG-NTR interactions depends on the density of the FG repeats. It is unclear how *in vitro* measurement conditions compare to *in vivo* densities of the FG-Nups, which are significantly lower in the cytoplasmic

and nucleoplasmic vestibules. Moreover, not all FG repeats may be simultaneously accessible, for example, for structural reasons or because they self-associate (Ribbeck and Görlich, 2001). And second, many *in vitro* binding affinities for NTRs likely do not reflect the affinity of a single FG repeat for an NTR, but rather significantly overestimate the strength of this binding interaction due to multiple interactions. To address this issue, a multivalent binding model used to explain nanomolar affinities predicted a substantially weaker affinity for a single NTR-FG interaction, even as weak as millimolar (Tetenbaum-Novatt *et al*, 2012), consistent with the weak NTR-FG interaction strengths predicted by our model.

The data and the analyses reported here also place constraints on existing models. For the nuclear import of M9- $\beta$ Gal-8C to occur rapidly, any interactions of the FG repeats with themselves, as required for the selective-phase/hydrogel model (Ribbeck and Görlich, 2001; Frey and Görlich, 2007), must be at most of similar magnitude to the interactions of FG repeats with transportin. If the FG-FG interactions were stronger, then transportin-FG interactions would not be strong enough to compensate for breaking FG-FG interactions, and the permeability barrier would be largely impenetrable. Nonetheless, even weak FG-FG interactions can significantly modulate FG-NTR interactions through density-dependent effects. The human NPC has  $\sim 3600$  FG repeats



(Stewart, 2007a; Peleg and Lim, 2010), which corresponds to a concentration of  $\sim 10\text{--}30\text{ mM}$ , depending on the assumptions about the spatial distribution of the FG repeats. For an FG–FG dissociation constant of  $K_D \approx 1\text{ mM}$  and a total FG concentration of  $\sim 30\text{ mM}$ ,  $\sim 80\%$  of the FG repeats would interact with each other at any given moment, yielding a low millimolar concentration of free, but not necessarily accessible, FG repeats. Lowering the concentration of free FG repeats in this way would reduce multivalent effects, reducing the apparent binding affinity. However, our multivalency picture and free energy potential model are also consistent with an alternative hypothesis in which FG self-interactions are minimal. For example, the permeability barrier could primarily result from the density of the FG polypeptides, e.g., confined in a polymer brush configuration (Lim *et al*, 2006). In such a model, FG–NTR interactions are necessary to overcome the entropic cost of displacing the FG polypeptides.

In the picture developed here, relatively weak interactions are needed to overcome the permeability barrier, thus predicting that various types of different weak and/or non-specific interactions would be sufficient for overcoming this barrier. Consistent with this idea, it has been shown that relatively small changes in the hydrophobicity of a protein are sufficient to overcome the permeability barrier (Naim *et al*, 2009), in agreement with our finding that an excess number of hydrophobic dye labels on the large M9- $\beta$ Gal cargo is sufficient to penetrate the permeability barrier (Supplementary Figure S2). In addition, weak charge interactions have been suggested to be important for NPC permeability (Colwell *et al*, 2010; Tagliazucchi *et al*, 2013). The overall interaction strength is likely to be determined by a combination of these and other relatively weak effects, such as the disruption of water solvation layers around FG repeats and NTRs during binding (Levy and Onuchic, 2006). However, the physical chemistry of these interactions is still poorly understood. Future investigations are required to further define the requirements for penetration into the FG network and to connect them to a molecular interactions picture. We hope that this work will encourage more controlled measurements of NTR–FG affinities.

## Materials and methods

### The M9- $\beta$ Gal-8C cargo

Beta-galactosidase ( $\beta$ Gal) is a homotetrameric sugar hydrolase (Juers *et al*, 2001). An M9 signal peptide was genetically linked to the N-terminus of each monomer (Lyman *et al*, 2002). To eliminate complications arising from binding to and/or hydrolysis of sugars within the NPC, two residues, E537Q (GAA  $\rightarrow$  CAA) and W999L (TGG  $\rightarrow$  CTG), at the catalytic site were mutated to reduce catalytic activity ( $k_{\text{cat}}$ ) by  $\sim 10^5$ -fold and increase the  $K_M$  by  $\sim 50$ -fold (Yuan *et al*, 1994; Huber *et al*, 2003). Two surface cysteines, C76A (TGC  $\rightarrow$  GCC) and C1021S (TGT  $\rightarrow$  TCT), were mutated to reduce the total number of surface accessible cysteines in the tetramer. All mutations were generated by the QuikChange protocol (Agilent Technologies), and were confirmed by DNA sequencing. The optimized cargo, M9- $\beta$ Gal-8C, has four M9 NLSs and is labelled with up to eight dye molecules under saturating conditions.

### Protein purification and labelling

Ran, NTF2, M9- $\beta$ Gal, and transportin were expressed and purified as described previously (Izaurralde *et al*, 1997; Lyman *et al*, 2002; Yang *et al*, 2004), except that for M9- $\beta$ Gal-8C, a French press was used to break cells and a Superose 6 size-exclusion column (10/300, GE Healthcare) was used as the last purification step. Transportin-

ybbR has a C-terminal ybbR13 tag (DSLEFIASKLA), confirmed by DNA sequencing. Alexa647 was enzymatically attached to the ybbR tag as described (see Supplementary data) (Yin *et al*, 2005, 2006). Protein concentrations were determined by SDS–PAGE using BSA as a standard. M9- $\beta$ Gal-8C was labelled with a 225-fold molar excess of Alexa647 maleimide (Yang *et al*, 2004). After labelling, the excess free dye was removed with Ni-NTA resin (Superflow, Qiagen). The eluate was concentrated with a 50-kD spin column (Microsep, Life Science) and further purified by Superose 6 size-exclusion chromatography. Cargo purification and labelling was performed within a single day to minimize aggregation. The mean labelling ratio was  $\sim 7.5$  dye molecules per tetramer, as determined by comparing the dye concentration (from the absorbance at 650 nm) to the protein concentration.

### Permeabilized cell assay

Cells were permeabilized and prepared for microscopy as previously described (Izaurralde *et al*, 1997; Lyman *et al*, 2002; Yang *et al*, 2004). In short, HeLa cells were grown on coverslips overnight, and  $\sim 20\text{ }\mu\text{L}$  flow chambers were constructed from high-vacuum grease and a top coverslip. Cells were permeabilized by incubation with  $40\text{ }\mu\text{g/ml}$  digitonin in import buffer (20 mM Hepes, 110 mM KOAc, 5 mM NaOAc, 2 mM MgOAc, 1 mM EGTA, pH 7.3) for 2 min. Permeabilized cells were washed three times with import buffer containing 1.5% (w/v) polyvinylpyrrolidone (PVP,  $\sim 360\,000\text{ g/mol}$ ). The reagent mix for import experiments was 1 mM GTP, 0.5  $\mu\text{M}$  RanGDP, 1  $\mu\text{M}$  transportin, 1  $\mu\text{M}$  NTF2, and cargo (250 nM in bulk and  $\sim 0.1\text{ nM}$  in single molecule experiments) in import buffer with 1.5% (w/v) PVP, unless otherwise indicated. RanGDP is converted into RanGTP by chromatin-bound RanGEF (RCC1) after transport into nuclei by NTF2 (Bischoff and Ponstingl, 1991).

### Microscopy

Confocal and narrow-field epifluorescence images were obtained on the same inverted microscope set-up (Zeiss Axiovert 200M) using a 1.46 NA  $\times 100$  oil-immersion objective (Zeiss alpha Plan-Apochromat). A spinning disk confocal microscopy attachment (Yokogawa) equipped with a CCD camera (Andor) was used to determine bulk nuclear import rates. Narrow-field epifluorescence microscopy (300  $\mu\text{m}$  excitation pinhole;  $\sim 1\text{ kW/cm}^2$  at 647 nm) (Yang and Musser, 2006b) was used for single molecule experiments. In short, the illumination area in a wide-field microscope set-up was confined to  $\sim 7\text{ }\mu\text{m}$  by the pinhole, increasing the signal-to-noise ratio sufficiently for single molecule detection. Green and far-red fluorescence channels were aligned to  $\sim 4\text{ nm}$ . Static precision for M9- $\beta$ Gal-8C was  $\sim 15\text{--}19\text{ nm}$  (see Supplementary data).

### Trajectory alignment

The criteria and methods used to select NPC interaction events and align trajectories were similar to those described previously (Yang *et al*, 2004; Yang and Musser, 2006a, b), with a few important changes, which we now describe. To determine the location of NPCs via fluorescence microscopy, a stable HeLa cell line was generated in which NPCs were tagged with GFP-rPom121, which consists of GFP N-terminally linked to rat Pom121 (see Supplementary data). The NE location was determined as described previously (Yang *et al*, 2004; Yang and Musser, 2006b), using the GFP fluorescence from EGFP-rPom121. Due to the very low observed transport efficiencies under some conditions, the trajectory selection rules were modified. Instead of selecting only trajectories that approached within 100 nm of a verified NE crossing point (at which at least one particle was observed to cross the NE), particles that approached within 100 nm of the measured NE position were considered to interact with an NPC. This approach will include some particles that did not interact with NPCs, but, based on control experiments without transportin, such events accounted for  $<10\%$  of those observed (Supplementary Table S1). Three types of abortive transport trajectories were observed: (i) particles that interacted at an NE location (within 100 nm) at which another particle crossed the NE, clearly establishing the presence of an NPC ( $\sim 25\%$ ); (ii) particles that crossed the NE and returned to the cytoplasm ( $\sim 50\%$ ); and (iii) particles that did not cross the NE plane, but did approach within 100 nm of the NE ( $\sim 25\%$ ). The NPC central axis was aligned to the above three

categories of trajectories as follows, respectively: (i) the NE crossing point for the entry event particle(s); (ii) the centroid of the trajectory points that were on the nuclear side of the NE; and (iii) the point of closest approach to the NE. Note that the location of the points at the beginning and the end of trajectories was often poorly defined due to diffusive motion. Only trajectories for which the location of trajectory end points *vis-à-vis* the NE was clearly identifiable were included in the analysis. However, poorly resolved end points were not included in trajectory overlays (Figure 3).

### Error analysis

Interaction time, import efficiency, and interaction frequency errors are standard errors of the mean ( $SD/N^{1/2}$ ). The standard deviation (SD) for the interaction time was determined from the graphing program (Origin) fitting routine. The SD for the import efficiency was calculated as  $[p(1-p)]^{1/2}$  according to the binomial distribution, where  $p$  is the experimentally measured import probability. The SD for the interaction frequency was calculated in the normal way from multiple measurements. For statistical significance, we used a two-tailed Welch's  $t$  test, which compares the mean of two populations that may have unequal variances.

## References

- Bayliss R, Littlewood T, Strawn LA, Wentz SR, Stewart M (2002) GLFG and FxFG nucleoporins bind to overlapping sites on importin- $\beta$ . *J Biol Chem* **277**: 50597–50606
- Bayliss R, Ribbeck K, Akin D, Kent HM, Feldherr CM, Görlich D, Stewart M (1999) Interaction between NTF2 and xFxFG-containing nucleoporins is required to mediate nuclear import of RanGDP. *J Mol Biol* **293**: 579–593
- Ben-Efraim I, Gerace L (2001) Gradient of increasing affinity of importin  $\beta$  for nucleoporins along the pathway of nuclear import. *J Cell Biol* **152**: 411–417
- Bischoff FR, Görlich D (1997) RanBP1 is crucial for the release of RanGTP from importin  $\beta$ -related nuclear transport factors. *FEBS Lett* **419**: 249–254
- Bischoff FR, Klebe C, Kretschmer J, Wittinghofer A, Ponstingl H (1994) RanGAP1 induces GTPase activity of nuclear Ras-related Ran. *Proc Natl Acad Sci USA* **91**: 2587–2591
- Bischoff FR, Ponstingl H (1991) Catalysis of guanine nucleotide exchange on Ran by the mitotic regulator RCC1. *Nature* **354**: 80–82
- Brohawn SG, Partridge JR, Whittle JRR, Schwartz TU (2009) The nuclear pore complex has entered the atomic age. *Structure* **17**: 1156–1168
- Chaillan-Huntington C, Braslavsky CV, Kuhlmann J, Stewart M (2000) Dissecting the interactions between NTF2, RanGTP, and the nucleoporin XFXFG repeats. *J Biol Chem* **275**: 5874–5879
- Chook YM, Blobel G (2001) Karyopherins and nuclear import. *Curr Opin Struct Biol* **11**: 703–715
- Chook YM, Stiel KE (2011) Nuclear import by karyopherin- $\beta$ s: recognition and inhibition. *Biochem Biophys Acta* **1813**: 1593–1606
- Colwell LJ, Brenner MP, Ribbeck K (2010) Charge as a selection criterion for translocation through the nuclear pore complex. *PLoS Comput Biol* **6**: e1000747
- de Gennes P (1979) *Scaling Concepts in Polymer Physics*. Ithaca, NY: Cornell University Press
- Dingwall C, Sharnick SV, Laskey RA (1982) A polypeptide domain that specifies migration of nucleoplasm into the nucleus. *Cell* **30**: 449–458
- Fahrenkrog B, Aebi U (2003) The nuclear pore complex: nucleocytoplasmic transport and beyond. *Nat Rev Mol Cell Biol* **4**: 757–766
- Feldherr CM, Kallenbach E, Schultz N (1984) Movement of karyophilic protein through the nuclear pores of oocytes. *J Cell Biol* **99**: 2216–2222
- Frey S, Görlich D (2007) A saturated FG-repeat hydrogel can reproduce the permeability properties of nuclear pore complexes. *Cell* **130**: 512–523
- Güttler T, Görlich D (2011) Ran-dependent nuclear export mediators: a structural perspective. *EMBO J* **30**: 3457–3474
- Huber RE, Hakda S, Cheng C, Cupples CG, Edwards RA (2003) Trp-999 of beta-galactosidase (*Escherichia coli*) is a key residue for binding, catalysis, and synthesis of allolactose, the natural lac operon inducer. *Biochemistry* **42**: 1796–1803
- Hülsmann BB, Labokha AA, Görlich D (2012) The permeability of reconstituted nuclear pores provides direct evidence for the selective phase model. *Cell* **150**: 738–751
- Hurt E, Strasser K, Segref A, Bailer SM, Schlaich N, Presutti C, Tollervy D, Jansen R (2000) Mex67p mediates nuclear export of a variety of RNA polymerase II transcripts. *J Biol Chem* **275**: 8361–8368
- Izaurrealde E, Kutay U, von Kobbe C, Mattaj IW, Görlich D (1997) The asymmetric distribution of the constituents of the Ran system is essential for transport into and out of the nucleus. *EMBO J* **16**: 6535–6547
- Jacobson RH, Zhang X-J, DuBose RF, Matthews BW (1994) Three-dimensional structure of  $\beta$ -galactosidase from *E. coli*. *Nature* **369**: 761–766
- Jamali T, Jamali Y, Mehrbod M, Mofrad MRK (2011) Nuclear pore complex: biochemistry and biophysics of nucleocytoplasmic transport in health and disease. *Int Rev Cell Mol Biol* **287**: 233–286
- Juere DH, Heightman TD, Vasella A, McCarter JD, Mackenzie L, Withers SG, Matthews BW (2001) A structural view of the action of *Escherichia coli* (lacZ) beta-galactosidase. *Biochemistry* **40**: 14781–14794
- Keminer O, Peters R (1999) Permeability of single nuclear pores. *Biophys J* **77**: 217–228
- Kindt TJ, Goldsby RA, Osborne IA, Kuby J (2007) *Immunology*. W. H. Freeman & Co., New York
- Kutay U, Bischoff FR, Kostka S, Kraft R, Görlich D (1997) Export of importin  $\alpha$  from the nucleus is mediated by a specific nuclear transport factor. *Cell* **90**: 1061–1071
- Levy Y, Onuchic JN (2006) Water mediation in protein folding and molecular recognition. *Ann Rev Biophys Biomol Struct* **35**: 389–415
- Lim RYH, Aebi U, Fahrenkrog B (2008a) Towards reconciling structure and function in the nuclear pore complex. *Histochem Cell Biol* **129**: 105–116
- Lim RYH, Huang N-P, Koser J, Deng J, Lau KHA, Schwarz-Herion K, Fahrenkrog B, Aebi U (2006) Flexible phenylalanine-glycine nucleoporins as entropic barriers to nucleocytoplasmic transport. *Proc Natl Acad Sci USA* **103**: 9512–9517
- Lim RYH, Ullman KS, Fahrenkrog B (2008b) Biology and biophysics of the nuclear pore complex and its components. *Int Rev Cell Mol Biol* **267**: 299–342
- Lyman SK, Guan T, Bednenko J, Wodrich H, Gerace L (2002) Influence of cargo size on Ran and energy requirements for nuclear protein import. *J Cell Biol* **159**: 55–67

### Supplementary data

Supplementary data are available at *The EMBO Journal* Online (<http://www.embojournal.org>).

## Acknowledgements

We thank Larry Gerace for the M9- $\beta$ Gal plasmid; Jan Ellenberg for the rPom121-3EGFP and pEGFP-Nup37 plasmids; Kaori Watanabe for purification of transportin, NTF2, and RanGDP, and the construction of transportin-ybBR; and Paul Cremer and Murray Stewart for thoughtful discussions. This work was supported by the NSERC, the NIH (GM084062), the DoD (N00014-02-1-0710), and the Welch Foundation (BE-1541).

**Author contributions:** The overall study was conceived and designed by L-CT and SMM. L-CT performed the experiments, with assistance from GF. L-CT, AZ, and SMM analysed the data. AZ and SMM derived the mathematical models. L-CT, AZ, and SMM wrote the paper.

## Conflict of interest

The authors declare that they have no conflict of interest.

- Ma J, Goryaynov A, Sarma A, Yang W (2012) Self-regulated viscous channel in the nuclear pore complex. *Proc Natl Acad Sci USA* **109**: 7326–7331
- Maimon T, Elad N, Dahan I, Medalia O (2012) The human nuclear pore complex as revealed by cryo-electron tomography. *Structure* **20**: 998–1006
- Mohr D, Frey S, Fischer T, Güttler T, Görlich D (2009) Characterization of the passive permeability barrier of nuclear pore complexes. *EMBO J* **28**: 2541–2553
- Naim B, Zbaida D, Dagan S, Kapon R, Reich Z (2009) Cargo surface hydrophobicity is sufficient to overcome the nuclear pore complex selectivity barrier. *EMBO J* **28**: 2697–2705
- Patel SS, Belmont BJ, Sante JM, Rexach MF (2007) Natively unfolded nucleoporins gate protein diffusion across the nuclear pore complex. *Cell* **129**: 83–96
- Peleg O, Lim RY (2010) Converging on the function of intrinsically disordered nucleoporins in the nuclear pore complex. *Biol Chem* **391**: 719–730
- Pyhtila B, Rexach M (2003) A gradient of affinity for the karyopherin Kap95p along the yeast nuclear pore complex. *J Biol Chem* **278**: 42699–42709
- Ribbeck K, Görlich D (2001) Kinetic analysis of translocation through nuclear pore complexes. *EMBO J* **20**: 1320–1330
- Ribbeck K, Görlich D (2002) The permeability barrier of nuclear pore complexes appears to operate via hydrophobic exclusion. *EMBO J* **21**: 2664–2671
- Richardson WD, Mills AD, Dilworth SM, Laskey RA, Dingwall C (1988) Nuclear protein migration involves two steps: rapid binding at the nuclear envelope followed by slower translocation through nuclear pores. *Cell* **52**: 655–664
- Rout MP, Aitchison JD, Suprapto A, Hjertaas K, Zhao Y, Chait BT (2000) The yeast nuclear pore complex: composition, architecture, and transport mechanism. *J Cell Biol* **148**: 635–651
- Siebrasse JP, Kaminski T, Kubitscheck U (2012) Nuclear export of single native mRNA molecules observed by light sheet fluorescence microscopy. *Proc Natl Acad Sci USA* **109**: 9426–9431
- Söderqvist H, Hallberg E (1994) The large C-terminal region of the integral pore membrane protein, POM121, is facing the nuclear pore complex. *Eur J Cell Biol* **64**: 186–191
- Stewart M (2007a) Molecular mechanism of the nuclear protein import cycle. *Nat Rev Mol Cell Biol* **8**: 195–208
- Stewart M (2007b) Ratcheting mRNA out of the nucleus. *Mol Cell* **25**: 327–330
- Stoffler D, Fahrenkrog B, Aebi U (1999) The nuclear pore complex: from molecular architecture to functional dynamics. *Curr Opin Cell Biol* **11**: 391–401
- Sun C, Fu G, Ciziene D, Stewart M, Musser SM (2013) Choreography of importin  $\alpha$ /CAS complex assembly and disassembly at the nuclear pore complex. *Proc Natl Acad Sci USA* **110**: E1584–E1593
- Sun C, Yang W, Tu L-C, Musser SM (2008) Single molecule measurements of importin  $\alpha$ /cargo complex dissociation at the nuclear pore. *Proc Natl Acad Sci USA* **105**: 8613–8618
- Suntharalingam M, Wentz SR (2003) Peering through the pore: nuclear pore complex structure, assembly, and function. *Dev Cell* **4**: 775–789
- Tagliazucchi M, Peleg O, Kröger M, Rabin Y, Szleifer I (2013) Effect of charge, hydrophobicity, and sequence of nucleoporins on the translocation of model particles through the nuclear pore complex. *Proc Natl Acad Sci USA* **110**: 3363–3368
- Tetenbaum-Novatt J, Hough LE, Mironska R, McKinney SA, Rout MP (2012) Nucleocytoplasmic transport: a role for nonspecific competition in karyopherin-nucleoporin interactions. *Mol Cell Proteomics* **11**: 31–46
- Tu L-C, Musser SM (2010) Single molecule studies of nucleocytoplasmic transport. *Biochim Biophys Acta* **1813**: 1607–1618
- Wentz SR, Rout MP (2010) The nuclear pore complex and nuclear transport. *Cold Spring Harb Perspect Biol* **2**: a000562
- Yamada J, Phillips JL, Patel S, Goldfien G, Calestagne-Morelli A, Huang H, Rexza R, Acheson J, Krishnan VV, Newsam S, Gopinathan A, Lau EY, Colvin ME, Uversky VN, Rexach MF (2010) A bimodal distribution of two distinct categories of intrinsically-disordered structures with separate functions in FG nucleoporins. *Mol Cell Proteomics* **9**: 2205–2224
- Yang W, Gelles J, Musser SM (2004) Imaging of single-molecule translocation through nuclear pore complexes. *Proc Natl Acad Sci USA* **101**: 12887–12892
- Yang W, Musser SM (2006a) Nuclear import time and transport efficiency depend on importin  $\beta$  concentration. *J Cell Biol* **174**: 951–961
- Yang W, Musser SM (2006b) Visualizing single molecules transiting through nuclear pore complexes with narrow-field epifluorescence microscopy. *Methods* **39**: 3316–3328
- Yin J, Lin AJ, Golan DE, Walsh CT (2006) Site-specific protein labeling by Sfp phosphopantetheinyl transferase. *Nat Protocols* **1**: 280–285
- Yin J, Straight PD, McLoughlin SM, Shou Z, Lin AJ, Golan DE, Kelleher NL, Kolter R, Walsh CT (2005) Genetically encoded short peptide tag for versatile protein labeling by Sfp phosphopantetheinyl transferase. *Proc Natl Acad Sci USA* **102**: 15815–15820
- Yuan J, Martinez-Bilbao M, Huber RE (1994) Substitutions for Glu-537 of beta-galactosidase from *Escherichia coli* cause large decreases in catalytic activity. *Biochem J* **299**: 527–531
- Zilman A, Di Talia S, Chait BT, Rout MP, Magnasco MO (2007) Efficiency, selectivity, and robustness of nucleocytoplasmic transport. *PLoS Comp Biol* **3**: 1281–1290

## SUPPLEMENTARY INFORMATION

### SUPPLEMENTARY MATERIALS AND METHODS

**Cell Line.** A plasmid expressing GFP N-terminally linked to rat Pom121 (GFP-rPom121) was made by replacing the hNUP37 gene in a plasmid encoding EGFP-hNUP37 with the rPom121 gene from a plasmid encoding rPom121-3EGFP using HindIII and MfeI restriction sites. Plasmids expressing rPom121-3EGFP and EGFP-hNUP37 were gifts from J. Ellenberg (European Molecular Biology Laboratory, Heidelberg, Germany) (2). The EGFP-rPom121 coding sequence was confirmed by DNA sequencing. HeLa cells were transfected with the EGFP-rPom121 plasmid as described previously (4). Stable transformants were selected with Geneticin (0.4 g/500 mL, Invitrogen). A single colony was chosen and amplified to yield a stable cell line. Transfected HeLa cells were grown at 37°C, 5% CO<sub>2</sub> in Dulbecco's Modified Eagle Medium (D-MEM, GIBCO) containing 10% fetal bovine serum (GIBCO) and 0.4 g/L Geneticin.

**Microscopy.** Confocal and narrow-field epifluorescence images were obtained on the same inverted microscope setup (Zeiss Axiovert 200M) using a 1.46 NA 100X oil-immersion objective (Zeiss alpha Plan-Apochromat). Attached to the left side-port was a spinning-disk confocal unit (Yokagawa CSU-X1) equipped with an optical fiber for the excitation beam and a 512x512 EMCCD camera (Andor iXon DU-897) for image acquisition. On the right side-port was a 128x128 EMCCD camera (Roper Scientific Cascade 128) used for narrow-field epifluorescence imaging (5). A 2.5 W ArKr mixed-gas ion laser (Spectra-Physics) was used for 488 and 647 nm excitation. Green (GFP, NPCs) and dark red (Alexa647, cargo) narrow-field epifluorescence images were collected at 40 and 500 Hz, respectively, on the same EMCCD camera. A typical single molecule experiment was comprised of a series of green-dark red-green images all collected within 1 min to minimize error due to stage drift ( $0.2 \pm 0.04$  nm/s). The NPC images at the beginning and end of the image series were compared to ensure that sample movement did not occur during acquisition. Permeabilized HeLa cells were prepared as described previously (5), and import experiments were performed in transport buffer [20 mM Hepes (pH 7.3), 110 mM KOAc, 5 mM NaOAc, 2 mM MgOAc, 1 mM EDTA, 1.5% polyvinylpyrrolidone (360 kDa, Sigma), and 2 mM dithiothreitol]. Photobleaching time for M9- $\beta$ Gal-8C was ~600 ms for most of the dyes (~80% reduction of initial emission intensity) and 800-1200 ms for complete photobleaching. Thus, photobleaching was essentially non-existent during imaging of NPC interaction times, which were < 10 ms.

**Image Alignment.** The image alignment error between fluorescence channels as determined with 0.1  $\mu$ m Tetraspeck microspheres (Invitrogen) was  $4 \pm 3$  nm ( $n = 24$ ). The low error likely results from the small fields aligned, an objective (Zeiss 440782-9800-000 alpha Plan-Apochromat 100x/1.46) with lower aberrations than previously used (1, 4, 5), and the use of a multibandpass dichroic/emission filter combination (Semrock Di01-R405/488/561/635-25x36 and FF01-446/523/600/677-25), which obviated a filter change between fluorescence channels. Density maps were generated using the "Contour" function of OriginLab software.

**Spatial Resolution.** Static spatial precision was determined by repeated position measurements of single coverslip-adsorbed molecules. Due to



photobleaching, the static spatial precision of M9- $\beta$ Gal-8C was  $\sim 15$  nm in the first  $\sim 80$  ms of observation and  $\sim 17$ - $19$  nm in the first 200 ms. The diffusion constant of M9- $\beta$ Gal-8C labeled with eight Alexa647 molecules was  $0.81 \pm 0.09 \mu\text{m}^2/\text{s}$  within the NPC (Figure S1), indicating that the average distance traveled during acquisition of 2 ms images was  $\sim 40$  nm. Thus, the localization precision for moving M9- $\beta$ Gal-8C molecules was  $\sim 43$ - $44$  nm, estimated as described earlier (3).

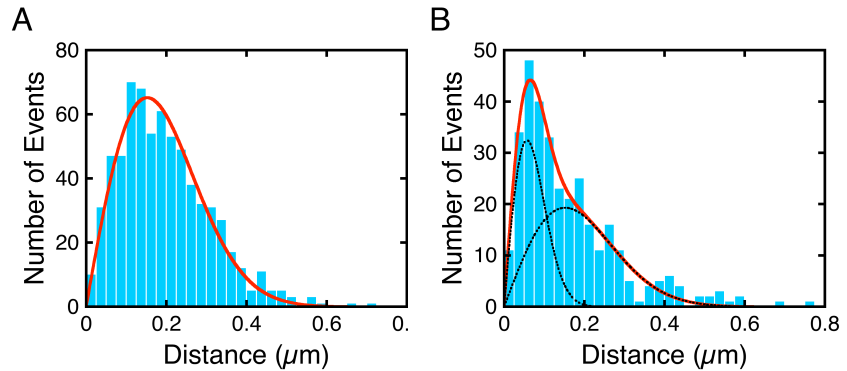


**Figure S1. Single-molecule diffusion measurements.** The diffusion constant of M9- $\beta$ Gal-8C labeled with eight Alexa647 molecules was obtained as described (1). (A) Frequency distribution of the distance traveled by an M9- $\beta$ Gal-8C molecule (saturated with transportin) in 2 ms within the cytoplasmic compartment of permeabilized cells (within  $\sim 5 \mu\text{m}$  of the NE). The data were fit to  $p(\delta, \tau, D) = A \cdot p(\delta, \tau, D)$ , yielding a diffusion constant  $D = 5.8 \pm 0.2 \mu\text{m}^2/\text{s}$ . (B) Frequency distribution of the distance traveled in 2 ms from the trajectories in Figure 3C. Data were fit to  $p(\delta, \tau, D_0, D_2) = A \cdot p(\delta, \tau, D_0) + B \cdot p(\delta, \tau, D_2)$ , yielding  $D_0 = 5.8 \pm 0.6 \mu\text{m}^2/\text{s}$  (61%) and  $D_2 = 0.81 \pm 0.09 \mu\text{m}^2/\text{s}$  (39%). Since  $D_0$  is identical to the cytoplasmic diffusion constant obtained in (A), it is assumed that  $D_2$  represents the diffusion constant of M9- $\beta$ Gal-8C when bound to the FG-network. [M9- $\beta$ Gal-8C] = 0.1 nM; [NTF2] = 1  $\mu\text{M}$ ; [RanGDP] = 0.5  $\mu\text{M}$ ; [GTP] = 1 mM; [transportin] = 1  $\mu\text{M}$ .

**The M9- $\beta$ -Galactosidase Model Cargo.** M9- $\beta$ Gal fully-labeled with 16 dye molecules translocated into nuclei in a signal-independent manner, indicating that large numbers of dye molecules can promote transport through the NPC. In addition, since  $\beta$ -Galactosidase is a disaccharide hydrolase (6), we were concerned that binding to and potential hydrolysis of polysaccharides within the NPC (7) would yield heterogeneous results and complicate interpretation. To address these issues, we reduced the number of dye labeling sites to 8 via two mutations (C76A and C1021S), and we reduced the  $\beta$ Gal catalytic activity ( $k_{cat}$ ) by  $\sim 10^5$ -fold and increased the  $K_M$  by  $\sim 50$ -fold with two mutations, E537Q and W999L (8, 9). We found that all four mutations were required to prevent signal-independent uptake of M9- $\beta$ Gal (Figure S2).

**Transport Complexes.** Gel filtration (Superose 6, Amersham-Pharmacia, optimal separation range 5-5000 kDa) was used to separate transport complexes from mixtures of transportin and M9- $\beta$ Gal-8C (unlabeled). When combined in  $\sim 25$ :1 ratio (transportin:cargo, T/C = 25), three major protein ( $A_{280}$ ) peaks eluted between 11 mL and 16 mL (Figure S3A, black curve), which roughly correlate to molecular weights of  $\sim 1$  MDa,  $\sim 500$  kDa and  $\sim 100$  kDa, respectively, based on the elution profile of protein standards (Gel Filtration Calibration Kits, GE Healthcare). The two lower molecular weight peaks are identified as M9- $\beta$ Gal-8C and transportin, respectively, based on the elution profiles of the pure proteins (Figure S3A, light blue ( $\beta$ ) and orange (T) curves). The highest molecular weight peak (T4 $\beta$ ) is consistent with M9- $\beta$ Gal-8C + 4 transportin molecules. Note that the largest protein standard used was thyroglobulin (670 kDa), and therefore, higher molecular weight peak assignments are approximate. To further support the T4 $\beta$  peak assignment, elution profiles of two additional mixtures were examined. For T/C = 1, the main peak

eluted at ~600 kDa, consistent with M9- $\beta$ Gal-8C + 1 transportin molecule (Figure S3B, dark blue curve, T1 $\beta$ ). For T/C = 3, the main peak eluted at ~900 kDa, consistent with M9- $\beta$ Gal-8C + 3 transportin molecules (Figure S3B, green curve, T3 $\beta$ ). No free transportin was found for these low T/C mixtures, consistent with a high binding affinity ( $K_D \approx 42$  nM (10)). These data indicate that the M9- $\beta$ Gal-8C is able to simultaneously bind 3-4 transportin molecules, and the transport complexes are stable enough to be resolved by size exclusion chromatography.

As an alternative approach to determine how many transportin molecules simultaneously bound to M9- $\beta$ Gal-8C, purified complexes were analyzed by stepwise photobleaching experiments (3). Transportin was modified at the C-terminus with a ybbR tag. This ybbR tag was covalently and specifically modified with a single CoA-Alexa647 dye molecule using Sfp phosphopantetheinyl transferase (11, 12). After enzymatic labeling of transportin-ybbR, the majority (>90%) of the unlinked CoA-Alexa647 was removed by one passage through a Zeba desalting column (2 mL, 7K MWCO, Thermo Scientific). The labeled transportin yields two fluorescent peaks upon Superose 6 gel chromatography (Figure S3C, red curve), consistent with

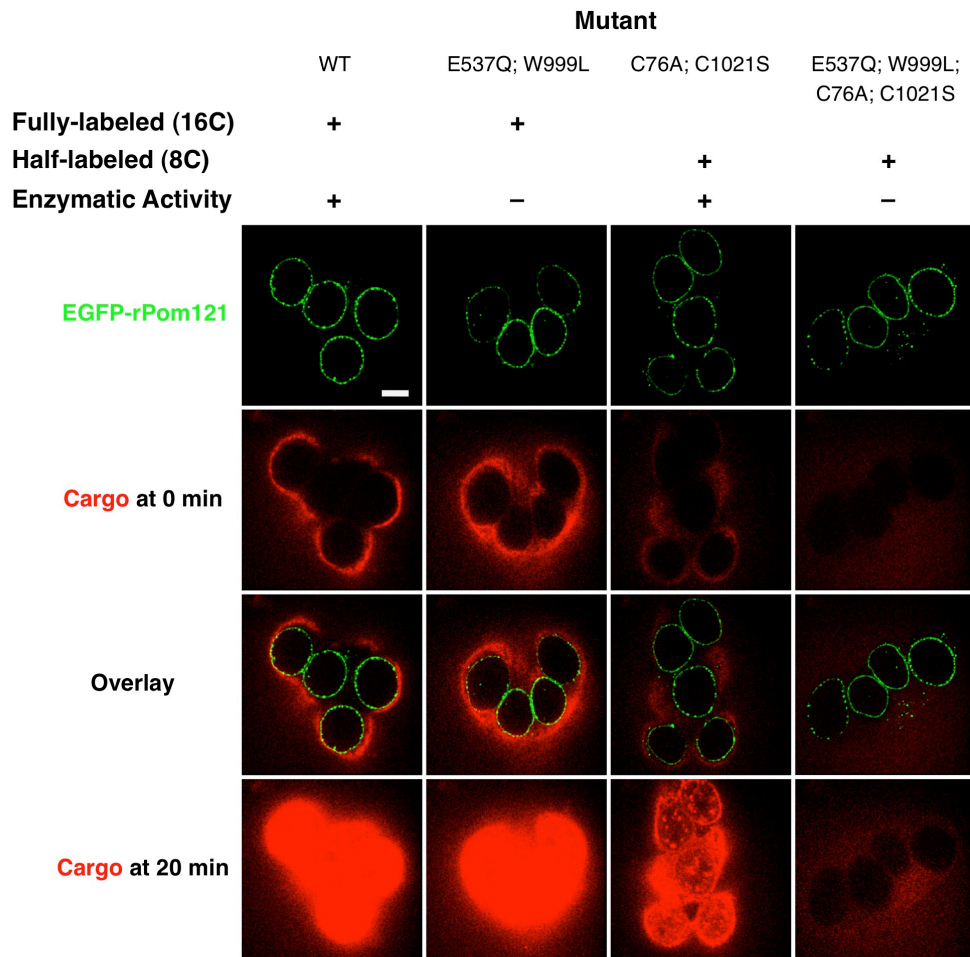


**Figure S2. Effects of Decreasing the Number of Dye Labels and Reducing Sugar Binding and Hydrolase Activities on the Nuclear Transport of M9- $\beta$ Gal.** Nuclear envelopes were visualized by EGFP-rPom121 fluorescence (*green*) and M9- $\beta$ Gal was visualized by Alexa647 fluorescence (*red*) using confocal microscopy. Fully-labeled wild-type M9- $\beta$ Gal (16C) binds to NPCs and enters the nucleoplasm of digitonin-permeabilized HeLa cells in the absence of transportin. Enzymatic mutations (E537Q and W999L) and cysteine mutations (C76A and C1021S), yielding M9- $\beta$ Gal-8C, are both required to prevent signal-independent nuclear uptake. See text for details. [M9- $\beta$ Gal] = 0.25  $\mu$ M. Scale bar, 10  $\mu$ m.

transportin-ybbR<sup>Alexa647</sup> (T') and free (unreacted) CoA-Alexa647 (CoA). Three protein elution peaks were observed when M9- $\beta$ Gal-8C and transportin-ybbR<sup>Alexa647</sup> were mixed (Figure S3C, violet curve, T/C = 8). The two lower molecular weight peaks are consistent with Sfp (~30 kDa) and free transportin-ybbR<sup>Alexa647</sup> (~100 kDa). The major peak at ~1 MDa is consistent with M9- $\beta$ Gal-8C + 3-4 transportin molecules (T'3 $\beta$ -T'4 $\beta$ ). The proteins in this peak were spread onto a microscope coverslip and imaged under stepwise photobleaching conditions (3) within 15 min after elution from the Superose 6 column (Figure S3D). Four distinct photobleach steps (and no more than 4) were observed for some fluorescent spots, supporting the hypothesis that M9- $\beta$ Gal-8C molecules can simultaneously bind up to four transportin molecules. The large number of spots that exhibited less than four photobleach steps is explained by incomplete dye labeling of transportin and/or complex decomposition after elution from the gel filtration column.

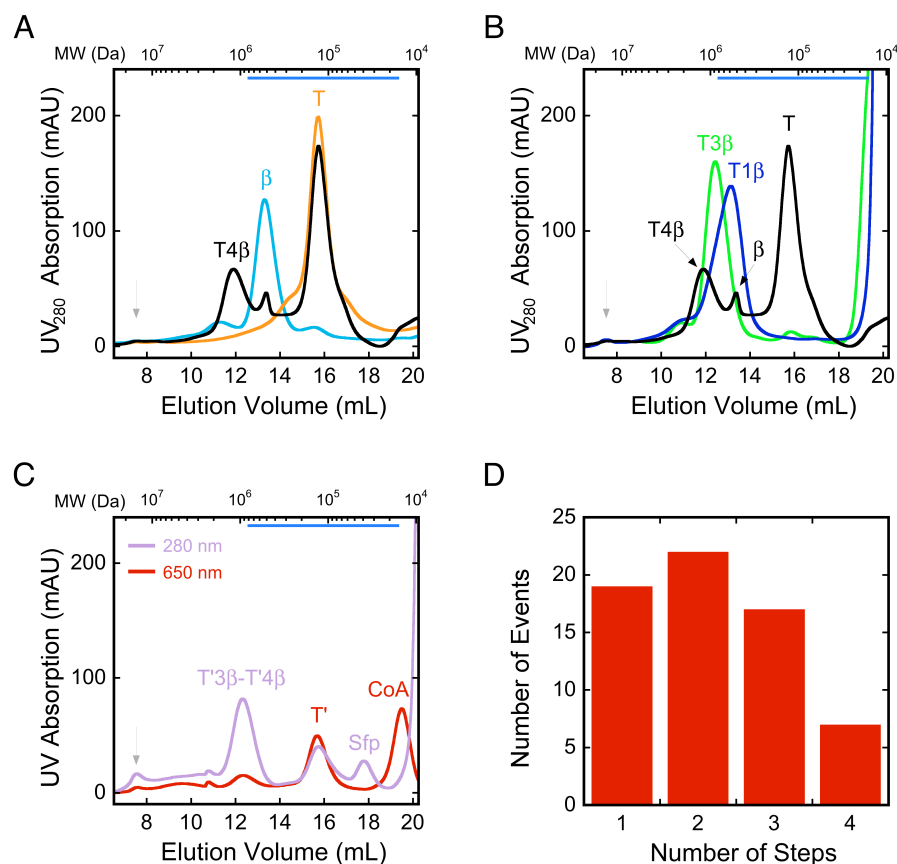


**Figure S3. Size Exclusion Gel Chromatography and Stepwise Photobleaching of M9- $\beta$ Gal-8C NTR-Cargo Complexes.** (A)-(C) Superose 6 gel filtration chromatography of transportin and the M9- $\beta$ Gal-8C cargo. Molecular weights based on 9 standard proteins (670 kDa to 13.7 kDa) are identified by the y-scale on the top, with the reliable region highlighted by the blue bar. The grey arrow indicates the void volume (> 5 MDa). Proteins were detected at 280 nm, unless otherwise indicated. The elution buffer was 50 mM Tris-HCl, 50 mM NaCl, 5 mM DTT (pH = 7.2). (A) Elution profile of a transportin:M9- $\beta$ Gal-8C mixture (T/C = 25, black). Elution profiles of M9- $\beta$ Gal-8C alone (light blue) and transportin alone (orange) are shown for comparison. (B) Elution profiles of T/C = 1 (dark blue) and 3 (green) transportin:M9- $\beta$ Gal-8C mixtures. The T/C = 25 elution profile from (A) is also shown (black) for comparison. (C) Elution profile of a transportin-ybbR<sup>Alexa647</sup>:M9- $\beta$ Gal-8C mixture (T/C = 8, violet). The elution profile of transportin-ybbR<sup>Alexa647</sup> monitored at 650 nm (detecting the Alexa647 dye) is shown for comparison (red). (D) Histogram of stepwise photobleaching events (3) observed for the T'3 $\beta$ -T'4 $\beta$  peak in (C) (N = 65). See text for details.

## SUPPLEMENTARY DISCUSSION

### EQUILIBRIUM THERMODYNAMICS OF MULTIVALENT BINDING

**Multivalent Affinity (Avidity).** Multivalency effects can be estimated as follows. This derivation is an extension of the approach followed by Yang et al (13). It is first assumed that each transportin molecule can interact with a single FG repeat. The result will then be expanded to multiple FG interactions per transportin molecule. For simplicity, it is assumed that the NTR-cargo complex of interest is the M9-βGal-8C cargo bound to four transportin molecules. If the NTR-cargo complex is in a homogeneous sea of FG repeats, the equilibria for the four sequential FG binding interactions are:

$$C + F \rightleftharpoons CF_1 \quad K_{D1} = \frac{k_{off(D1)}}{k_{on(D1)}} = \frac{[C][F]}{[CF_1]} \quad (3)$$

$$CF_1 + F \rightleftharpoons CF_2 \quad K_{D2} = \frac{k_{off(D2)}}{k_{on(D2)}} = \frac{[CF_1][F]}{[CF_2]} \quad (4)$$

$$CF_2 + F \rightleftharpoons CF_3 \quad K_{D3} = \frac{k_{off(D3)}}{k_{on(D3)}} = \frac{[CF_2][F]}{[CF_3]} \quad (5)$$

$$CF_3 + F \rightleftharpoons CF_4 \quad K_{D4} = \frac{k_{off(D4)}}{k_{on(D4)}} = \frac{[CF_3][F]}{[CF_4]} \quad (6)$$

where  $C$  and  $F$  represent the NTR-cargo complex and the FG repeats, respectively. Mass balance yields:

$$C_0 = [C] + [CF_1] + [CF_2] + [CF_3] + [CF_4] \quad (7)$$

where  $C_0$  represents the initial concentration of the NTR-cargo complex. Solving in terms of  $[C]$  and  $[F]$  using Eqs. 3-6 yields:

$$C_0 = [C] + \frac{[C][F]}{K_{D1}} + \frac{[C][F]^2}{K_{D1}K_{D2}} + \frac{[C][F]^3}{K_{D1}K_{D2}K_{D3}} + \frac{[C][F]^4}{K_{D1}K_{D2}K_{D3}K_{D4}} \quad (8)$$

With a single transportin molecule in the NTR-cargo complex, the fraction of complexes bound to an FG repeat is given by:

$$\frac{[CF]}{C_0} = \frac{[F]}{K_{D1(1)} + [F]} \quad (9)$$

which is obtained by substituting  $[C] = C_0 - [CF_1]$  into Eq. 3, and is a typical Langmuir binding isotherm. Here we include a parenthetical 1 in the  $K_{D1}$  term to indicate the binding affinity when there is only one transportin molecule in the NTR-cargo complex. As discussed below, the value of  $K_{D1}$  depends on the number of NTRs in the cargo complex. Analogously, the fraction of NTR-cargo complexes containing four transportin molecules that are bound to at least one FG repeat is:



$$\frac{[CF_1] + [CF_2] + [CF_3] + [CF_4]}{C_0} = \frac{C_0 - [C]}{C_0} = \frac{[F]}{K_{app} + [F]} \quad (10)$$

or, using Eq. 8:

$$\frac{C_0 - [C]}{C_0} = \frac{[F]}{\frac{K_{D1(4)} K_{D2} K_{D3} K_{D4}}{K_{D2} K_{D3} K_{D4} + K_{D3} K_{D4} [F] + K_{D4} [F]^2 + [F]^3} + [F]} \quad (11)$$

where we have used  $K_{D1(4)}$ , which represents the initial binding affinity when there are four transportin molecules in the NTR-cargo complex. Formally, as described below, parenthetical numbers should be used for all the  $K_D$ 's, but most are omitted for clarity. Eq. 11 is of the same form as Eq. 9, indicating that the apparent  $K_D$ , which describes the apparent affinity of an NTR-cargo complex with four transportin receptors for the FG-network, is:

$$K_{app} = \frac{K_{D1(4)} K_{D2} K_{D3} K_{D4}}{K_{D2} K_{D3} K_{D4} + K_{D3} K_{D4} [F] + K_{D4} [F]^2 + [F]^3} \quad (12)$$

or:

$$\frac{K_{app}}{K_{D1(4)}} = \frac{1}{1 + \frac{[F]}{K_{D2}} + \frac{[F]^2}{K_{D2} K_{D3}} + \frac{[F]^3}{K_{D2} K_{D3} K_{D4}}} \quad (13)$$

Note that  $K_{app}$  depends on each of the individual binding affinities and the FG concentration. Eq. 13 corresponds to Eq. 1 in the main text.

**Binding and Unbinding Rates.** Differences in affinities implies differences in the local binding and unbinding rates of the NTR-cargo complexes from the FG-network. The equilibrium constants can be written in terms of kinetic rate constants as follows:

$$K_{D1(1)} = \frac{k_{off}}{k_{on}} \quad (14)$$

$$K_{D1(4)} = \frac{k_{off}}{4k_{on}} \quad (15)$$

where  $k_{off}$  and  $k_{on}$  are the intrinsic off- and on-times of a single FG repeat for a single binding site, and where, as mentioned earlier, the parenthetical numbers reflect the number of transportin molecules in the NTR-cargo complex. The on-rate for the NTR-cargo complex with four transportin molecules is four times higher due to the additional binding sites, which explains the differences in interaction frequencies at different transport: cargo ratios (Figure 2E). Similarly, the on-rates and off-rates for other binding and unbinding events is determined by the number of available FG binding sites:

$$\frac{1}{4} k_{on(D1)} = \frac{1}{3} k_{on(D2)} = \frac{1}{2} k_{on(D3)} = k_{on(D4)} = k_{on} \quad (16)$$

$$k_{off} = k_{off(D1)} = \frac{1}{2} k_{off(D2)} = \frac{1}{3} k_{off(D3)} = \frac{1}{4} k_{off(D4)} \quad (17)$$

The relationships between  $K_{D2}$ ,  $K_{D3}$ , and  $K_{D4}$  can be estimated from Eqs. 16 and 17:

$$K_{D2} = \frac{4}{9} K_{D3} \quad (18)$$

$$K_{D2} = \frac{1}{6} K_{D4} \quad (19)$$

The apparent affinity, which includes the effect of multivalent interactions, can be written as:

$$K_{app} = \frac{k_{app}}{4k_{on}} \quad (20)$$

where  $k_{app}$  is the overall rate of release of all forms of the bound complexes to yield the FG-free complex. The ratio of off-times ( $\tau = 1/k$ ) at high and low transportin concentrations can be estimated as:

$$\frac{\tau_{app}}{\tau_{off}} = \frac{k_{off}}{k_{app}} = \frac{K_{D1}}{K_{app}} \quad (21)$$

Thus,  $K_{app}/K_{D1}$  provides a measure of the effect of multivalency not only on the equilibrium binding affinity but also on the local unbinding times. If  $K_{app}/K_{D1} < 1$ , multivalent interactions lead to a higher binding affinity and a slower release rate. Combining Eqs. 13, 18, 19, and 22, the ratio of off-times in the presence and absence of multivalency is given by:

$$\frac{\tau_{app}}{\tau_{off}} = 1 + \left( \frac{[F]}{K_{D2}} \right) + \frac{4}{9} \left( \frac{[F]}{K_{D2}} \right)^2 + \frac{2}{27} \left( \frac{[F]}{K_{D2}} \right)^3 \quad (22)$$

which is equation (2) in the main text, and which agrees with Hlavacek et al. (14). Note that the local fluctuations in  $[F]$  due to the dissociation of FG-FG interactions as the FG-network undergoes structural rearrangements to accommodate the cargo complex has not been accounted for here. These effects are expected to be small relatively to the major enthalpic effects of multivalency that are described by the multiple  $K$ 's. The multivalency effects for multiple  $[F]$  and  $K_{D2}$  values are summarized in Figure 4.

**Effect of Multiple FG Binding Sites on a Transportin Molecule.** It is certainly possibly that transportin molecules contain more than one FG binding motif. Molecular dynamics simulations suggest that NTRs contain  $\geq 6$  sites that weakly interact with FG repeats (15-17), although only one primary and one secondary binding site were detected in crystallographic experiments on importin  $\beta 1$  (18). If one binding motif dominates over all others, multivalent effects should be largely predicted by the simple one binding site model (Eq. 22). On the other hand, if the multiple binding sites have similar affinities, the derivation is readily extended by increasing the number of binding equilibria. The general form of Eq. 22 is:

$$\frac{\tau_{app}}{\tau_{off}} = 1 + \sum_{i=1}^{4n-1} \left( \frac{2}{4n-1} \right)^i \left( \frac{(4n-1)(4n-2)\dots(4n-i)}{(i+1)!} \right) \left( \frac{[F]}{K_{D2}} \right)^i \quad (23)$$

where  $n$  is the number of FG binding sites on a transportin molecule. Following the lead for a similar derivation (14), Eq. 23 can also be written in terms of  $K (= k_{off}/k_{on})$ ,

which is the intrinsic affinity of a single binding site on an NTR-cargo complex for an FG repeat:

$$\frac{\tau_{app}}{\tau_{off}} = 1 + \sum_{i=1}^{4n-1} \frac{(4n-1)(4n-2)\dots(4n-i)}{(i+1)!} \left( \frac{[F]}{K} \right)^i \quad (24)$$

The effect of additional binding sites is illustrated in Figure S4. Comparison of Figure S4A with Figure 4 illustrates that the relationship between  $[F]$  and  $K_{D2}$  is much more important in determining  $\tau_{app}/\tau_{off}$  than the number of FG binding sites on the NTR. In contrast, the number of FG binding sites significantly modulates the effect of  $K$  on  $\tau_{app}/\tau_{off}$  (Figures S4B and S4C).

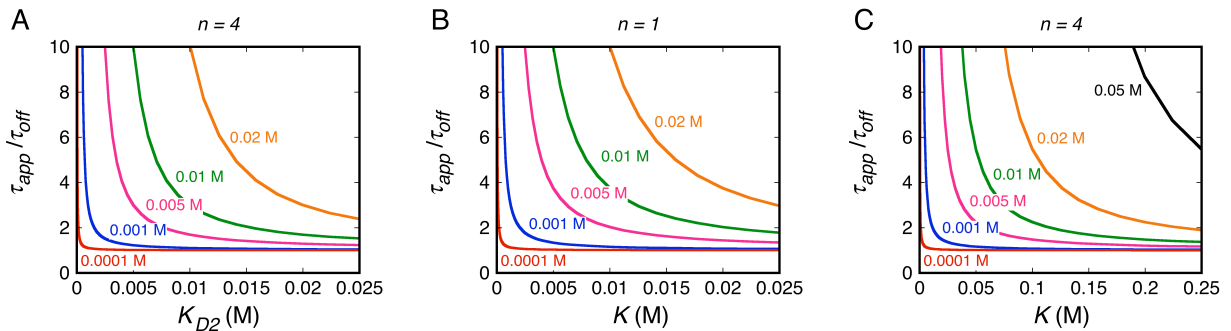


**Figure S4. Effect of  $[F]$  on  $\tau_{app}/\tau_{off}$ .** (A)  $\tau_{app}/\tau_{off}$  vs  $K_{D2}$  for  $n = 4$  according to equation 23. Compare with Figure 4. (B & C)  $\tau_{app}/\tau_{off}$  vs  $K$  for  $n = 1$  and  $n = 4$ , as indicated, according to equation 24. Note the different abscissa scale for C. The different  $[F]$  values for the various curves are identified in color.

**Implications.** While the lifetimes in Eqs. 22-24 describe the average time for the complex to release from the FG-network, they do not accurately reflect the time required to escape from the NPC (which is what is obtained from interaction time measurements in single molecule experiments) since the latter includes the time to diffuse through and out of the FG-network in the NPC, which could be significant. Nonetheless, Eqs. 22-24 indicate conditions under which multivalency is expected to be significant, namely, when  $[F] > K_{D2}$ . The data in Figure 2D reveal similar lifetimes for NTR-cargo complexes with 1-4 bound transportin molecules, indicating similar off-times, and thus, that multivalency effects are weak for the M9- $\beta$ Gal-8C cargo bound to four transportin molecules. This presents a serious conundrum since the total FG concentration in the central pore is normally estimated to be around 30 mM (19, 20) and NTR affinities for an FG repeat are typically estimated to be in the micromolar range or less (21-28). The solution may include some combination of the following: 1) the accessible or apparent FG concentration in the NPC is significantly lower than the total predicted FG concentration, e.g. due to FG-FG interactions, immobility, and/or a larger (less dense) FG cloud than anticipated; and 2) the FG affinity is strongly dependent on context, e.g., on the structural arrangement within the network and/or the energetic cost of disrupting the FG-network.

## DIFFUSION IN AN EFFECTIVE POTENTIAL

**Transport Efficiency.** We assume that the movement of a cargo molecule through the NPC can be described as simple diffusion in an effective potential (Figure 6). There are several ways to calculate transport efficiency for this model that are more or less equivalent up to numerical prefactors that depend on the detailed assumptions of the dynamics near the pore entrance. The transport efficiency, i.e., the probability that a particle at  $y_1$  reaches position  $y_5$  (as opposed to  $y_0$ ), is given by the following expression (29, 30):

$$P_{tr}(U) = \frac{\int_{y_0}^{y_1} \frac{e^{U(y)}}{D(y)} dy}{\int_{y_0}^{y_5} \frac{e^{U(y)}}{D(y)} dy} \quad (25)$$

where  $U$  is the potential energy and  $D$  is the diffusion constant of the particle. In the absence of RanGTP,

$$P_{tr}^{-Ran}(U) = \frac{1}{2 + 2 \left[ \frac{D_0 x_1}{D_1 x_0} e^{E_v} + \frac{D_0 x_2}{D_2 x_0} e^{E_b} \right]} \quad (26)$$

where  $D_0$ ,  $D_1$ , and  $D_2$  are the diffusion constants in the cytoplasm and the nucleoplasm, in the cytoplasmic and nucleoplasmic vestibules, and in the central permeability barrier, respectively. In the presence of RanGTP,

$$P_{tr}^{+Ran}(U) = \frac{1}{1 + e^{E_{Ran}} + \frac{D_0 x_1}{D_1 x_0} \left( \frac{3}{2} e^{E_v} + \frac{1}{2} e^{E_{Ran}} \right) + \frac{2D_0 x_2}{D_2 x_0} e^{E_b}} \quad (27)$$

where we have assumed that RanGTP starts to act, on average, in the middle of the nucleoplasmic vestibule (Figure 6B). Assuming  $D_0 = 5.8 \mu\text{m}^2/\text{s}$  and  $D_2 = 0.8 \mu\text{m}^2/\text{s}$  (Figure S1), and that  $D_1$  is approximately an average of  $D_0$  and  $D_2$  (i.e.,  $3.3 \mu\text{m}^2/\text{s}$ ),  $P_{tr}$  is shown for various well depths and barrier heights in Figures 6 and S5 in both the absence and presence of RanGTP.

**Interaction Time.** An NTR-cargo complex's average interaction time with the NPC was described by Zilman et al (29). The mean interaction time,  $\tau(U)$ , depends both on the translocation time of cargos that pass through the pore and the time that cargos undergoing abortive transport spend at the pore, as described earlier (29-31). Here, we use the alternate expression:

$$\tau(U) = P_{tr}(U) \int_{y_0}^{y_5} \frac{e^{U(y)}}{D(y)} dy \int_{y_0}^y e^{-U(x)} dx - \int_{y_0}^{y_1} \frac{e^{U(y)}}{D(y)} dy \int_{y_0}^y e^{-U(x)} dx \quad (28)$$

where the limits refer to the model in Figure 6. Eq. 28 reduces to equation S(1) in the Zilman et al. paper after some term rearrangements. The mean interaction times in the absence and presence of RanGTP, respectively, are given by:



$$\tau(-Ran) = P_{tr}^{-Ran} \left[ \frac{2x_0}{D_0} (x_0 + x_1 e^{-E_v} + x_2 e^{-E_b}) + \frac{2x_1}{D_1} (x_0 e^{E_v} + x_1 + x_2 e^{E_v - E_b}) + \frac{2x_2}{D_2} (x_0 e^{E_b} + x_1 e^{E_b - E_v} + x_2) \right] - \frac{x_0^2}{2D_0} \quad (29)$$

$$\tau(+Ran) = P_{tr}^{+Ran} \left[ \frac{x_0}{D_0} \left[ x_0 (1 + e^{E_{Ran}}) + x_1 \left( \frac{1}{2} + \frac{3}{2} e^{E_{Ran} - E_v} \right) + 2x_2 e^{E_{Ran} - E_b} \right] + \frac{x_1}{D_1} \left( x_0 \left( \frac{3}{2} e^{E_v} + \frac{1}{2} e^{E_{Ran}} \right) + x_1 \left( \frac{5}{4} + \frac{3}{4} e^{E_{Ran} - E_v} \right) + x_2 (e^{E_v - E_b} + e^{E_{Ran} - E_b}) \right) + \frac{2x_2}{D_2} (x_0 e^{E_b} + x_1 e^{E_b - E_v} + x_2) \right] - \frac{x_0^2}{2D_0} \quad (30)$$

Assuming the diffusion constants discussed earlier,  $\tau$  is shown for various well depths and barrier heights in Figures 6 and S5 in both the absence and presence of RanGTP.

#### Axial Length of the FG-Nup "Cloud."

In the discussion thus far, we have assumed that the axial length of the FG-Nup "cloud," the distance between the edges of the cytoplasmic and nucleoplasmic vestibules furthest from the NPC center, is 200 nm, i.e.,  $2x_1 + 2x_2 = 200$  nm. We also examined the predicted effect of multivalency on transport efficiency and interaction times for  $2x_1 + 2x_2 = 80$  nm (Figure S6). The central barrier width was again assumed to be 20 or 40 nm, but the vestibule widths were changed to 30 or 20 nm, respectively. These narrower vestibules may more accurately reflect the arrangement of the FG-Nup cloud within the NPC if all of the

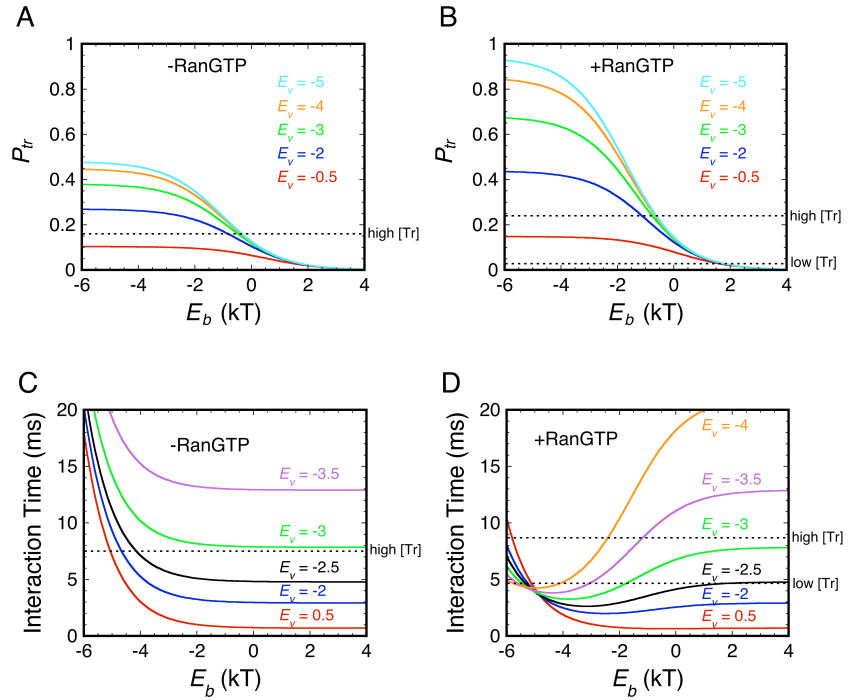
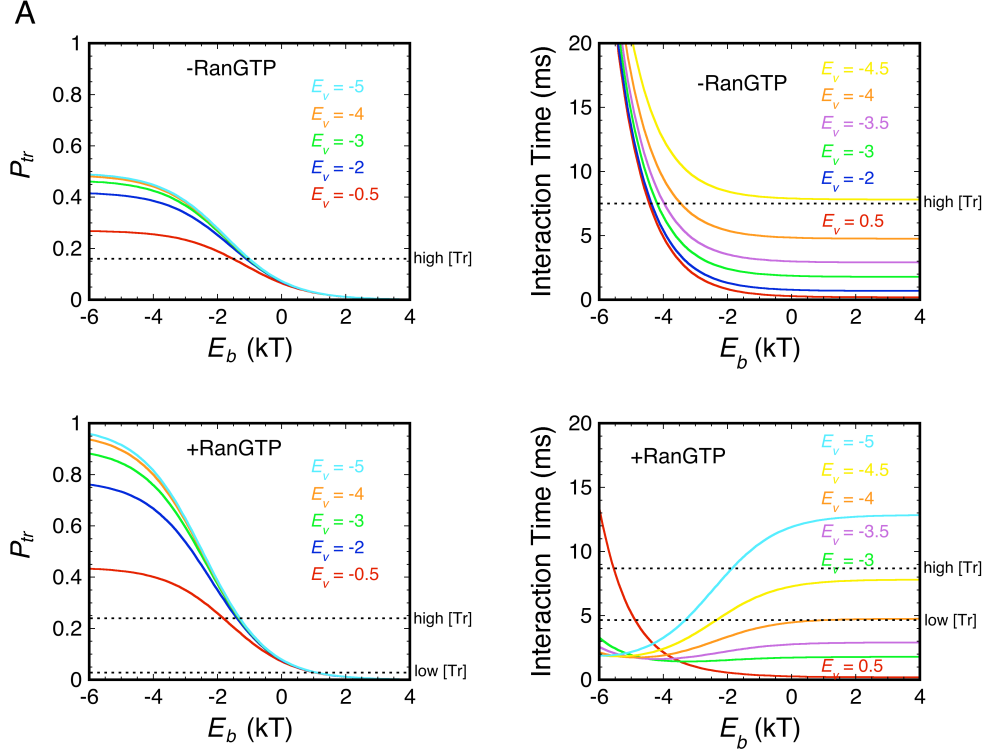


**Figure S5. Transport efficiency ( $P_{tr}$ ) and mean interaction time ( $\tau$ ) as a function of the barrier height ( $E_b$ ) for various well depths ( $E_v$ ), assuming a barrier width ( $2x_2$ ), vestibule width ( $x_1$ ), and escape distance ( $x_0$ ) of 20, 90 and 25 nm, respectively.** Comparison with Figure 6, in which a 40 nm barrier width was assumed, reveals only small differences. Experimentally determined values (Table S1) are indicated for low and high transportin (Tr) concentrations in the presence and absence of RanGTP by the horizontal dashed lines, as indicated.

FG-polypeptides are tethered to the core NPC scaffold and none are tethered to the cytoplasmic filaments or nuclear basket. Comparison with the data suggest barrier heights in the presence and absence of RanGTP similar to what was obtained earlier for the wider vestibules, but the vestibule depths are  $\sim 1-1.5 k_B T$  deeper. The depths and widths of the vestibules primarily control interaction time, as this is where the cargo complexes spend most of the time, and transport probability is controlled primarily by the barrier height.

### 40 nm Barrier



### 20 nm Barrier

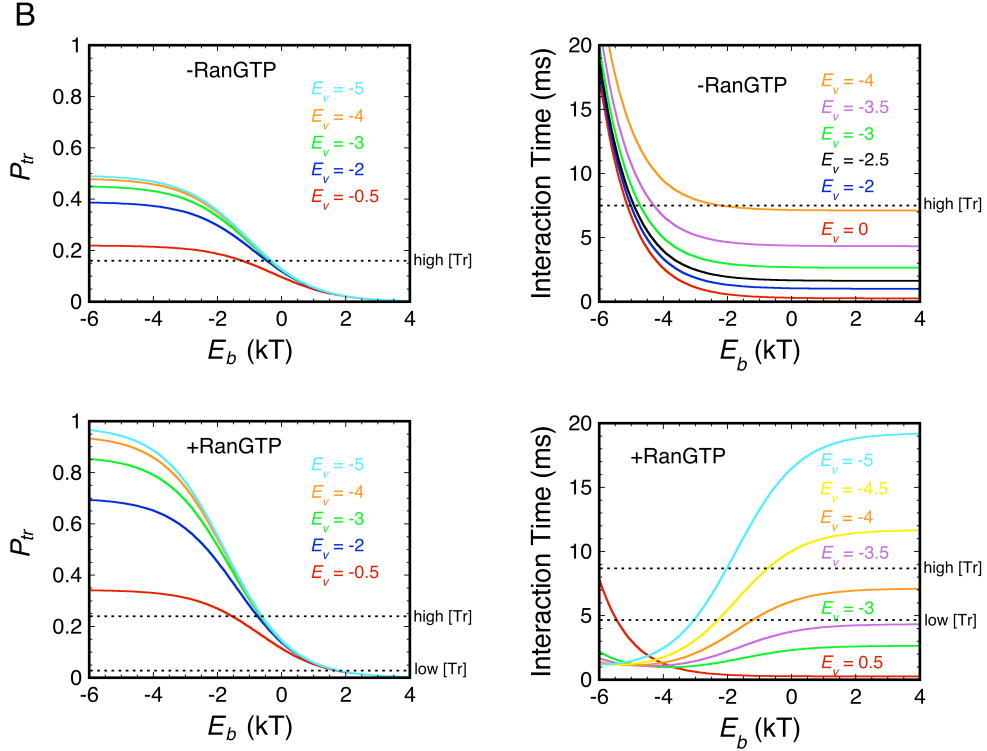


**Figure S6. Transport efficiency ( $P_{tr}$ ) and mean interaction time ( $\tau$ ) as a function of the barrier height ( $E_b$ ) for various well depths ( $E_v$ ), assuming an FG-Nup cloud of 80 nm.** (A) The barrier width ( $2x_2$ ), vestibule width ( $x_1$ ) and escape distance ( $x_0$ ) are 40, 20 and 25 nm, respectively. (B) The barrier width ( $2x_2$ ), vestibule width ( $x_1$ ) and escape distance ( $x_0$ ) are 20, 30 and 25 nm, respectively. Experimentally determined values (Table S1) are indicated for low and high transportin (Tr) concentrations in the presence of absence and RanGTP by the horizontal dashed lines, as indicated. Comparison with Figures 6, S5 and S6, in which the FG-Nup cloud was 200 nm, reveals similar barrier heights under the various experimental conditions, but vestibule depths  $\sim 1$ - $1.5 k_B T$  lower.

## SUPPLEMENTARY REFERENCES

1. Yang W, Musser SM (2006) Nuclear import time and transport efficiency depend on importin  $\beta$  concentration. *J. Cell Biol.* 174:951-961.
2. Rabut G, Doye V, Ellenberg J (2004) Mapping the dynamic organization of the nuclear pore complex inside single living cells. *Nat. Cell Biol.* 6:1114-1121.
3. Yang W, Musser SM (2006) Visualizing single molecules transiting through nuclear pore complexes with narrow-field epifluorescence microscopy. *Methods* 39:3316-3328.
4. Sun C, Yang W, Tu L-C, Musser SM (2008) Single molecule measurements of importin  $\alpha$ /cargo complex dissociation at the nuclear pore. *Proc. Natl. Acad. Sci. USA* 105:8613-8618.
5. Yang W, Gelles J, Musser SM (2004) Imaging of single-molecule translocation through nuclear pore complexes. *Proc. Natl. Acad. Sci. USA* 101:12887-12892.
6. Juers DH, *et al.* (2001) A structural view of the action of *Escherichia coli* (lacZ) beta-galactosidase. *Biochemistry* 40:14781-14794.
7. Panté N, Aebi U (1994) Towards the molecular details of the nuclear pore complex. *J. Struct. Biol.* 113:179-189.
8. Huber RE, Hakda S, Cheng C, Cupples CG, Edwards RA (2003) Trp-999 of beta-galactosidase (*Escherichia coli*) is a key residue for binding, catalysis, and synthesis of allolactose, the natural lac operon inducer. *Biochemistry* 42:1796-1803.
9. Yuan J, Martinez-Bilbao M, Huber RE (1994) Substitutions for Glu-537 of beta-galactosidase from *Escherichia coli* cause large decreases in catalytic activity. *Biochem. J.* 299:527-531.
10. Lee BJ, *et al.* (2006) Rules for nuclear localization sequence recognition by karyopherin  $\beta$ 2. *Cell* 126:543-558.
11. Yin J, Lin AJ, Golan DE, Walsh CT (2006) Site-specific protein labeling by Sfp phosphopantetheinyl transferase. *Nat. Protocols* 1:280-285.
12. Yin J, *et al.* (2005) Genetically encoded short peptide tag for versatile protein labeling by Sfp phosphopantetheinyl transferase. *Proc. Natl. Acad. Sci. USA* 102:15815-15820.
13. Yang T, Baryshnikova OK, Mao H, Holden MA, Cremer PS (2003) Investigations of bivalent antibody binding on fluid-supported phospholipid membranes: the effect of hapten density. *J. Am. Chem. Soc.* 125:4779-4784.
14. Hlavacek WS, Percus JK, Percus OE, Perelson AS, Wofsy C (2002) Retention of antigen on follicular dendritic cells and B lymphocytes through complement-mediated multivalent ligand-receptor interactions: theory and application to HIV treatment. *Math. Biosci.* 176:185-202.



15. Isgro TA, Schulten K (2005) Binding dynamics of isolated nucleoporin repeat regions to importin-beta. *Structure* 13(12):1869-1879.
16. Isgro TA, Schulten K (2007) Association of nuclear pore FG-repeat domains to NTF2 import and export complexes. *J. Mol. Biol.* 266:330-345.
17. Isgro TA, Schulten K (2007) Cse1p-binding dynamics reveal a binding pattern for FG-repeat nucleoporins on transport receptors. *Structure* 15(8):977-991.
18. Bayliss R, Littlewood T, Stewart M (2000) Structural basis for the interaction between FxFG nucleoporin repeats and importin  $\beta$  in nuclear trafficking. *Cell* 102:99-108.
19. Peleg O, Lim RY (2010) Converging on the function of intrinsically disordered nucleoporins in the nuclear pore complex. *Biol. Chem.* 391(7):719-730.
20. Stewart M (2007) Molecular mechanism of the nuclear protein import cycle. *Nat. Rev. Mol. Cell Biol.* 8:195-208.
21. Ben-Efraim I, Gerace L (2001) Gradient of increasing affinity of importin  $\beta$  for nucleoporins along the pathway of nuclear import. *J. Cell Biol.* 152:411-417.
22. Gilchrist D, Mykytka B, Rexach M (2002) Accelerating the rate of disassembly of karyopherin•cargo complexes. *J. Biol. Chem.* 277:18161-18172.
23. Pyhtila B, Rexach M (2003) A gradient of affinity for the karyopherin Kap95p along the yeast nuclear pore complex. *J. Biol. Chem.* 278:42699-42709.
24. Lott K, Bhardwaj A, Mitrousis G, Pante N, Cingolani G (2012) The importin  $\beta$  binding domain modulates the avidity of importin  $\beta$  for the nuclear pore complex. *J. Biol. Chem.* 285:13769-13780.
25. Bayliss R, Littlewood T, Strawn LA, Wentz SR, Stewart M (2002) GLFG and FxFG nucleoporins bind to overlapping sites on importin- $\beta$ . *J. Biol. Chem.* 277:50597-50606.
26. Bayliss R, *et al.* (1999) Interaction between NTF2 and xFxFG-containing nucleoporins is required to mediate nuclear import of RanGDP. *J. Mol. Biol.* 293:579-593.
27. Tetenbaum-Novatt J, Hough LE, Mironska R, McKinney SA, Rout MP (2012) Nucleocytoplasmic transport: a role for nonspecific competition in karyopherin-nucleoporin interactions. *Mol. Cell. Proteomics* 11:31-46.
28. Ribbeck K, Görlich D (2001) Kinetic analysis of translocation through nuclear pore complexes. *EMBO J.* 20:1320-1330.
29. Zilman A, Di Talia S, Chait BT, Rout MP, Magnasco MO (2007) Efficiency, selectivity, and robustness of nucleocytoplasmic transport. *PLoS Comp. Biol.* 3:1281-1290.
30. Gardiner CW (2004) *Handbook of Stochastic Methods for Physics, Chemistry and the Natural Sciences* (Springer-Verlag).

31. Berezhkovskii AM, Pustovoi MA, Bezrukov SM (2003) Channel-facilitated membrane transport: average lifetimes in the channel. *J. Chem. Phys.* 119:3943.

**Table S1: Single Molecule Statistics for Nuclear Import of M9-βGal-8C at Different Transportin Concentrations<sup>1</sup>**

Transportin to M9-βGal-8C Ratio	RanGTP <sup>2</sup>	Interaction Time (ms)	<i>N</i> <sup>3</sup>	Import Efficiency (%)	<i>N</i> <sup>4</sup>	NE Interaction Frequency (events μm <sup>-1</sup> s <sup>-1</sup> )	<i>N</i> <sup>5</sup>	Cargo Oligomerization State <sup>6</sup> C:CT <sub>1</sub> :CT <sub>2</sub> :CT <sub>3</sub> :CT <sub>4</sub> (% of total)	CT <sub>2</sub> + CT <sub>3</sub> + CT <sub>4</sub> (% of total)
0:1	+					0.08 ± 0.03	4		
1:4	+	4.8 ± 0.4	198	3 ± 2	59	0.8 ± 0.1	4	78 : 20 : 2.0 : 0.09 : < 0.01	2.1 %
1:4	-					0.2 ± 0.1	3		
1:4 (pre-washed with RanGTP) <sup>7</sup>	+					0.6 ± 0.2	3		
1:4 (pre-washed with RanGTP) <sup>7</sup>	-					0.1 ± 0.1	3		
1:1	+	6.1 ± 0.5	212	13 ± 3	103	1.3 ± 0.2	3	32 : 42 : 21 : 4.5 : 0.36	26 %
4:1	+	7.5 ± 0.6	200	21 ± 3	151	2.0 ± 0.3	3	0.04 : 0.97 : 8.9 : 36 : 54	99 %
5,000:1	+	7.3 ± 1.2	77	21 ± 3	136	2.3 ± 0.2	3	< 0.01 : 0.17 : 3.1 : 24 : 72	99%
10,000:1	+	8.7 ± 0.8	198	24 ± 4	135	2.2 ± 0.1	3	< 0.01 : 0.03 : 0.90 : 14 : 85	100%
10,000:1	-	7.5 ± 0.6	238	16 ± 3	129	2.3 ± 0.4	4		
10,000:1 (pre-washed with transportin) <sup>8</sup>	-	5.6 ± 0.5	185	15 ± 5	62	0.8 ± 0.3	3		

<sup>1</sup>Unless otherwise noted, concentrations during single molecule import experiments were: [M9-βGal-8C] = ~0.1 nM, [NTF2] = 1 μM.

<sup>2</sup>When present, the RanGTP concentration was 0.5 μM (shorthand notation for 0.5 μM RanGDP + 1 mM GTP).

<sup>3</sup>*N* (number of events) for the interaction time.

<sup>4</sup>*N* (number of events) for the import efficiency.

<sup>5</sup>*N* (number of cells) for the interaction frequency.

<sup>6</sup>Theoretical cargo oligomerization states were calculated based on a binomial distribution using an M9-transportin dissociation constant of 42 nM (10) to estimate binding probability. For the two highest transportin: cargo ratios, the cargo was simply diluted into transport buffer containing 0.5 or 1  $\mu$ M transportin, and incubated for  $\geq 20$  min on ice before adding to permeabilized cells. For the three lowest ratios, transportin and cargo were first mixed at a higher concentration (0.2-2  $\mu$ M transportin) to speed binding and mitigate loss by adsorption to the vessel walls. After a  $\geq 20$  min incubation on ice, the solution was diluted to a final cargo concentration of  $\sim 0.1$  nM, and experiments were completed within 3 min after dilution. The oligomerization state distribution was calculated for the higher concentration, and therefore conservatively estimates the number of M9-transportin interactions (highest possible number of interactions, disregarding potential dissociation upon dilution).

<sup>7</sup>Permeabilized cells were preincubated with 0.5  $\mu$ M RanGTP for 10 min.

<sup>8</sup>Permeabilized cells were preincubated with 0.5  $\mu$ M transportin for 10 min. Pre-incubation of nuclei with transportin to dissociate endogenous RanGTP from NPCs resulted in a shorter interaction time and decreased interaction frequency, but did not affect the import efficiency. These data indicate that some import events are RanGTP independent. Under these conditions, excess transportin that binds to NPCs dissociates slowly (not shown), suggesting that RanGTP is not required for transportin to dissociate from NPCs, and that transportin accumulates at NPCs in the absence of RanGTP. The decreased interaction frequency can be explained by NPC-bound transportin interfering with the binding of incoming cargo complexes.



## Videos

For both videos, the pixel size is ~240 nm, each frame was acquired in 2 ms, and playback speed is 5 frames per second.

**Video 1)** Movie of the abortive event shown in Fig. 1C (top). (*green*) GFP (EGFP-rPom121) fluorescence intensity; (*red*) cargo (M9- $\beta$ Gal-8C-Alexa647) fluorescence intensity.

**Video 2)** Movie of the entry event shown in Fig. 1C (bottom). (*green*) GFP (EGFP-rPom121) fluorescence intensity; (*red*) cargo (M9- $\beta$ Gal-8C-Alexa647) fluorescence intensity.